



Study on unified strength theory and elastic–plastic stress update algorithm

Jinfu Ke

Received: 3 January 2024 / Accepted: 28 July 2024
© The Author(s) 2024

Abstract The unified strength theory with the two-piecewise linear equations is more convenient and concise to calculate the strength of materials. It can fully explore the potential in the strength of materials and improve the economic benefits of engineering design. This study combines the semi-implicit return mapping algorithm and the Aitken accelerated iteration scheme and develops a plastic constitutive algorithm for isotropic softening materials based on the unified strength theory. The combining method can simplify the stress update and make the calculation of consistent tangent modulus easier. Furthermore, it can avoid solving the partial derivatives of the plastic flow rule and overcome the stress-deviating problem. The self-developed constitutive algorithm is used to simulate the elastic–plastic excavation process of a deep-lying circular tunnel. The numerical simulation results match well with the theoretical solution, verifying the correctness of the self-developed constitutive algorithm. Based on the self-developed constitutive algorithm, the stability of an underground mining stope is comprehensively analyzed, and its structural

parameters are optimized. The research reveals the mechanism of stope instability, provides a reliable scientific basis for the mining design and decision-making, ensures the safe and efficient production of the stope, and achieves the expected goal.

Highlights

- Review of the shear strength theory of rock material.
- A new elastic–plastic stress update algorithm for the unified strength theory.
- Applications to underground stope’s stability analysis and optimization.

Keywords Unified strength theory · Elastic–plastic stress update algorithm · Semi-implicit return mapping algorithm · Aitken accelerated iteration scheme

1 Introduction

The strength of rock mass refers to the ultimate bearing capacity of the combined material of the rock and the weakening interior structure. The rock strength theory only includes the strength of undamaged material, but the influence of weakening interior structure on the strength of intact rock is excluded. Therefore,

J. Ke (✉)
Quanzhou Institute of Equipment Manufacturing, Haixi Institutes, Chinese Academy of Sciences, Jinjiang 362200, Fujian, China
e-mail: kejinfu@fjirms.ac.cn; kejinfu@hotmail.com

J. Ke
University of Chinese Academy of Sciences, Beijing 100049, China

the strength of rock refers to the ultimate bearing capacity of an intact rock specimen under all complex stress states. The Mohr–Coulomb strength theory proposed in 1900 has a dominant role in developing geotechnical mechanics and is one of the primary rock strength theories. In this more than a century of development, many scholars have conducted experiments to revise the Mohr–Coulomb strength theory, meanwhile they progressed many new rock strength theories (Walton et al. 2015; Yu 2018).

Under low confining compression stress, the mechanical behavior of rock is essentially a brittle failure, and the brittle failure of rock induces shearing dilatancy. However, the brittle failure converts into ductile failure under high confining compression stress, and the ductile failure stimulates shearing shrinkage. Mogi (1966) studied the transition point between the brittle failure and the ductile failure of rock and observed that the average ratio of axial compression stress to confining compression stress is between 3.4 and 4.3 when the transition happens. Hoek (1983), Hoek and Brown (1997) used a straightforward standard to judge the brittle failure of rock mass by assuming that the brittle failure occurs if the confining compression stress is less than the uniaxial compression strength of rock mass. Besides, they restricted the Hoek–Brown empirical strength criterion to the threshold that the confining compression stress must be less than half of the uniaxial compression strength.

This research deals with the strength theory related to plastic shear yielding, which induces the brittle failure of rock. According to the multi-shear yielding proposed by Yu et al. (2000, 2004), the strength theory can be divided into single-shear strength theory, double-shear strength theory, triple-shear strength theory, and various empirical strength criteria. The former three types all have clear physical significance. In this study, the stress uses the mathematical symbolic representation defined in material mechanics by assuming that the tensile stress is positive. Oppositely, the mathematical symbolic representation defined in rock mechanics is reversed.

Based on the classical soil unloading model, cavity expansion theory, and unified strength theory under large strain conditions, Wu et al. (2022) studied the influence of the soil unloading effect on compaction grouting and proposed a compaction grouting diffusion model considering the soil unloading effect, they also derived and verified the theoretical relationship between the soil unloading degree and the soil deformation modulus. According to the unified strength

theory, the equilibrium state of ultimate stress, and the theory of elastic mechanics clamped beam, Chen et al. (2022) established the arbitrary point stress calculation model, derived the stress solution of the clay soil under the action of gravity, and obtained the formula for calculating the critical radius of cavity induced by water and sand gushing. Based on the unified strength theory, Sun et al. (2022) studied the analytical solutions for the responses of the intermediate principal stress on the strain-softening rock behavior under excavated tunnels and investigated the influence of the elastic strain expressions on the tunnel responses. Gao and Li (2023) applied the unified strength theory to study the displacement and stress distribution in plastic zones of the tunnel surrounding rock. They concluded that the proper application of unified strength theory will guarantee the safety of engineering practice and have more practical value. The unified strength theory constitutive model was embedded in the secondary development of Abaqus to investigate the effect of soil-structure interaction on the seismic response of frame buildings on collapsible loess and develop a new nonlinear elastic model generated by the unified strength theory (Xiong et al. 2023). Based on the unified strength theory and the true triaxial test data of the fourteen rock types reported in the literature, Li et al. (2023) developed a generalized unified strength theory by introducing a mobilized factor to characterize the weakening effect of rock strength under high pressure. Wang et al. (2023) proposed a new numerical model based on the generalized nonlinear unified strength theory, verified the empirical formula for determining the parameter b by practical engineering, and concluded that the unified strength theory has good applicability to practical rock engineering and can provide guidance and reference for similar rock projects. Liu et al. (2023) used the twin-shear unified strength theory to calculate the active earth pressure. Considering the influence of intermediate principal stress, their research has theoretical significance and considerable engineering economic benefits. Zhang and Sun (2023). considered the intermediate principal stress effect of soils and applied the unified strength theory to correct the shear strength index of soils. Their research showed that the relative error of the slope stability coefficient could reach 39.87% due to the underestimation of the shear strength of soils and the missing effect of intermediate principal stress. Miao et al. (2024) developed a new

calculation method that uses the unified strength theory to improve the accuracy and reliability of the ultimate bearing capacity of reinforced concrete beams.

In our work, based on the unified strength theory, we develop a new combination method by combining the semi-implicit return mapping algorithm and the Aitken accelerated iteration scheme in the plastic constitutive algorithm for isotropic softening materials. The new combination method has a solid convergence and excellent applicability. The self-developed constitutive algorithm is used to simulate the elastic–plastic excavation of a deep-lying circular tunnel, and then it is applied to optimize structural parameters of a stope with mining practice. This research is split into seven major sections. Apart from the introduction, a review of the shear strength theory of rock material and the unified strength theory are presented in Sect. 2. The new proposed method is particularly described in Sect. 3. The effectiveness of the proposed approach is evaluated by numerical models and engineering applications in Sect. 4, Sect. 5, and Sect. 6, respectively. Finally, the main conclusions are drawn.

2 The shear strength theory of hard brittle material

2.1 Single-shear strength theories

The single-shear strength theory only takes the maximum shear stress and its correlative normal stress as the plastic shear yielding criterion.

According to the Mohr–Coulomb strength theory, among the three principal stresses, only the maximum and minimum principal stresses influence the plastic shear yielding behavior of materials. By using the principal stresses, the Mohr–Coulomb strength theory is expressed as follows:

$$\begin{cases} \tau_{13} + \sigma_{13} \sin \varphi = c \cos \varphi \\ \tau_{13} = (\sigma_1 - \sigma_3)/2, \quad \sigma_{13} = (\sigma_1 + \sigma_3)/2 \end{cases} \quad (1)$$

where c is the cohesive strength, φ is the internal friction angle, τ_{13} is the maximum shear stress, σ_{13} is the normal stress on the acting surface of the maximum shear stress, σ_1 is the maximum principal stress, σ_2 is the intermediate principal stress, and σ_3 is the minimum principal stress. According to the Mohr–Coulomb strength theory, the uniaxial compressive strength σ_c and uniaxial tensile strength σ_t of the material can be obtained as follows:

$$\sigma_c = \frac{2c \cos \varphi}{1 - \sin \varphi}, \quad \sigma_t = \frac{2c \cos \varphi}{1 + \sin \varphi} \quad (2)$$

The Mohr–Coulomb yielding surface is the inner boundary of all externally convex yielding surfaces, and its corresponding physical model is the hexahedron element of maximum shear stress (see Fig. 1).

In recent years, experimental studies on the brittle failure of hard rock under low confining compression stress show that the friction strength and the bonding strength do not act simultaneously. Furthermore, in the progressively brittle failure of hard rock, the friction strength generates its matching effect only when the intergranular bonding strength gradually weakens (Hajiabdolmajid and Kaiser 2003; Hajiabdolmajid et al. 2002, 2003).

The microscopic brittle failure mechanism shows that the intergranular bonding force decreases throughout the initial crack propagation. After the crack surfaces coalesce, the friction force is generated. Besides, the cracks propagate parallelly to the excavation boundary, causing surrounding rock to spall and fall of. Based on the mechanism that the friction strength strengthening and the bonding strength weakening, Hajiabdolmajid and Kaiser (2003), Hajiabdolmajid et al. (2002, 2003) introduced a rock brittleness indicator I_{Be} related to the equivalent plastic strain ϵ^p (see Fig. 2) and proposed the CWFS model as follows:

$$\begin{cases} \tau = c(\epsilon^p) + \sigma_n(\epsilon^p) \tan \varphi \\ I_{Be} = \frac{\epsilon_f^p - \epsilon_c^p}{\epsilon_c^p} \end{cases} \quad (3)$$

where ϵ_c^p is the equivalent plastic strain when the bonding strength reaches its residual value, and ϵ_f^p is

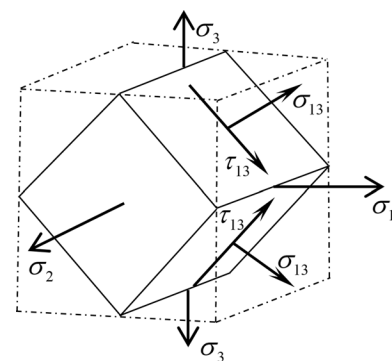


Fig. 1 Single-shear stress model

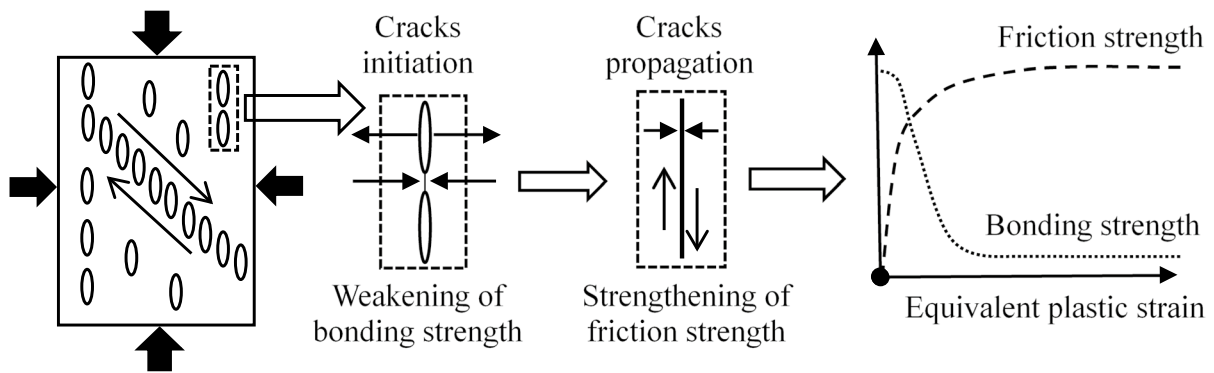


Fig. 2 The CWFS model

the equivalent plastic strain when the friction strength reaches its maximum strengthening value.

Qiao et al. (2012) stated that the friction strength is not only dependent on the normal stress σ_n but also related to the friction coefficient $\tan \varphi$ on the crack surface, which is controlled by the roughness of the closed crack surface. Furthermore, when the micro-cracks accumulate but not reach penetration yet, the increase of crack surface roughness and friction coefficient is small, and the change can be negligible. Nevertheless, when the crack is closed, the friction coefficient increases rapidly, the normal stress on the crack surface is effectively transferred, and the friction strength is mobilized.

However, the Mohr–Coulomb strength theory does not consider the influence of the intermediate principal stress σ_2 on the strength of the material. Moreover, many true triaxial experiments of rock materials show that the influence of intermediate principal stress σ_2 on material yielding and failure is up to 20–50% (Gao and Tao 1993). By combining the hydrostatic stress and the maximum shear stress to reflect the influence of intermediate principal stress, a generalized single-shear stress theory was proposed to improve the Mohr–Coulomb theory as follows (Yu et al. 2000, 2004; Labuz and Zang 2012):

$$\begin{cases} \tau_{13} + A\sigma_m = C \\ \sigma_m = (\sigma_1 + \sigma_2 + \sigma_3)/3 \end{cases} \quad (4)$$

where σ_m is the average principal stress, A and C are the undetermined material parameters.

Moreover, the effect of intermediate principal stress σ_2 on yielding is segmented. Further research showed that as the value of σ_2 increased from σ_3 to σ_1 ,

the material strength would increase to a peak value and then begin to gradually decrease (Mogi 1967, 1971; Yu 2004). This physical phenomenon is known as the piecewise effect of the intermediate principal stress on the strength of materials.

Single-shear strength theories have common defects since they do not consider the influence of intermediate principal stress on the strength of the material. Besides, the single-shear strength theories unable to characterize the piecewise effect of the intermediate principal stress on the strength of the material. Thus, they underestimate the material strength and cannot maximize the material potential (Yu et al. 2006, 2009; Yu and Li 2012; Yu 2018).

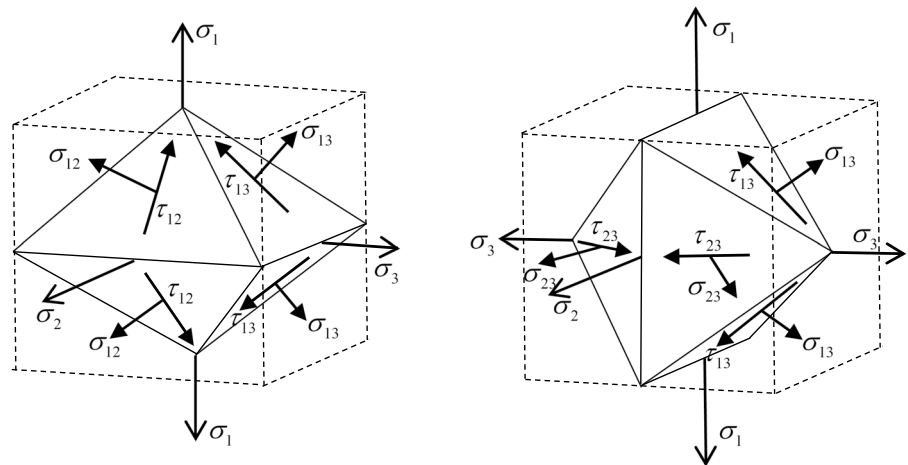
In conclusion, new theories must be developed because of those deficiencies, leading to the double-shear strength theories, triple-shear strength theories, and various empirical strength criteria.

2.2 Double-shear strength theories (the unified strength theory)

The three principal stresses can be converted to three principal shear stresses and three matching normal stresses. The double-shear strength theories are the shear strength theories that take only two principal shear stresses and corresponding normal stresses as the material plastic yielding criterion.

Yu et al. (2000) proposed the unified strength theory (see Fig. 3) to consider the piecewise effect of the intermediate principal stress on the material strength. Based on the double-shear stress models, meanwhile, with the help of the two principal shear stresses and

Fig. 3 Double-shear stress models



corresponding normal stresses, they obtained the mathematical expression of the unified strength theory as follows:

$$\begin{cases} \tau_{13} + \beta\sigma_{13} + b(\tau_{12} + \beta\sigma_{12}) = C, & \tau_{12} + \beta\sigma_{12} \geq \tau_{23} + \beta\sigma_{23} \\ \tau_{13} + \beta\sigma_{13} + b(\tau_{23} + \beta\sigma_{23}) = C, & \tau_{12} + \beta\sigma_{12} < \tau_{23} + \beta\sigma_{23} \\ \tau_{23} = (\sigma_2 - \sigma_3)/2, & \sigma_{23} = (\sigma_2 + \sigma_3)/2 \\ \tau_{12} = (\sigma_1 - \sigma_2)/2, & \sigma_{12} = (\sigma_1 + \sigma_2)/2 \end{cases} \quad (5)$$

where b is the double-shear parameter of rock. In different lithology, the influence of intermediate principal stress on the strength of the material is dissimilar, so the value of b is different. In conformity to the uniaxial tensile strength σ_t and uniaxial compression strength σ_c , we obtain expressions: $\alpha = (1 - \beta)/(1 + \beta) = \sigma_t/\sigma_c$ and $C = (1 + b)\sigma_c/(1 + \alpha)$. Substituting the above results into Eq. (5), we get the following expression:

$$\begin{cases} \sigma_1 - \frac{\alpha}{1+b}(b\sigma_2 + \sigma_3) = \sigma_t, & \sigma_2 \leq \frac{\sigma_1 + \alpha\sigma_3}{1+\alpha} \\ \frac{1}{1+b}(\sigma_1 + b\sigma_2) - \alpha\sigma_3 = \sigma_t, & \sigma_2 > \frac{\sigma_1 + \alpha\sigma_3}{1+\alpha} \end{cases} \quad (6)$$

Using the three stress invariants (I_1, J_2, θ) , the unified strength theory can be expressed as follows:

$$\begin{cases} F_1 = \frac{1-\alpha}{3}I_1 + \sqrt{J_2} \left[\frac{2+\alpha}{\sqrt{3}} \cos \theta + \frac{\alpha(1-b)}{(1+b)} \sin \theta \right] = \sigma_t, & F_1 \geq F_2 \\ F_2 = \frac{1-\alpha}{3}I_1 + \sqrt{J_2} \left[\left(\alpha + \frac{2-b}{1+b} \right) \frac{\cos \theta}{\sqrt{3}} + \left(\alpha + \frac{b}{1+b} \right) \sin \theta \right] = \sigma_t, & F_1 < F_2 \\ I_1 = \sigma_1 + \sigma_2 + \sigma_3, & J_2 = \frac{2}{3}(\tau_{13}^2 + \tau_{12}^2 + \tau_{23}^2), & \theta = \arccos\left(\frac{\tau_{13} + \tau_{12}}{\sqrt{3}J_2}\right) \in \left[0, \frac{\pi}{3}\right] \end{cases} \quad (7)$$

where θ is the spatial stress angle in the principal stress space.

The double-shear strength theory rationally reflects the piecewise effect of the intermediate principal stress on the material strength. Moreover, with reasonable values of parameters α and b , the unified strength theory can be degraded to many frequently used strength theories (see Fig. 4) as follows:

1. If $b = 0$, and then the unified strength theory degrades into the Mohr–Coulomb criterion $F_1 = F_2 = \sigma_1 - \alpha\sigma_3 = \sigma_t$.
2. If $b = 1$, the unified strength theory is degraded to the twin-shear strength theory proposed by Yu in 1985 and becomes the outer boundary of all external convex yielding surfaces.
3. If $b > 1$ or $b < 0$, the unified strength theory is degraded to the concave strength theory.
4. If $\alpha = 1$, the tension and compression strength of unified strength theory are equal, which is more suitable for traditional metal materials.

Figure 5 describes the yielding surface of the unified strength theory and its various special cases in the principal stress space.

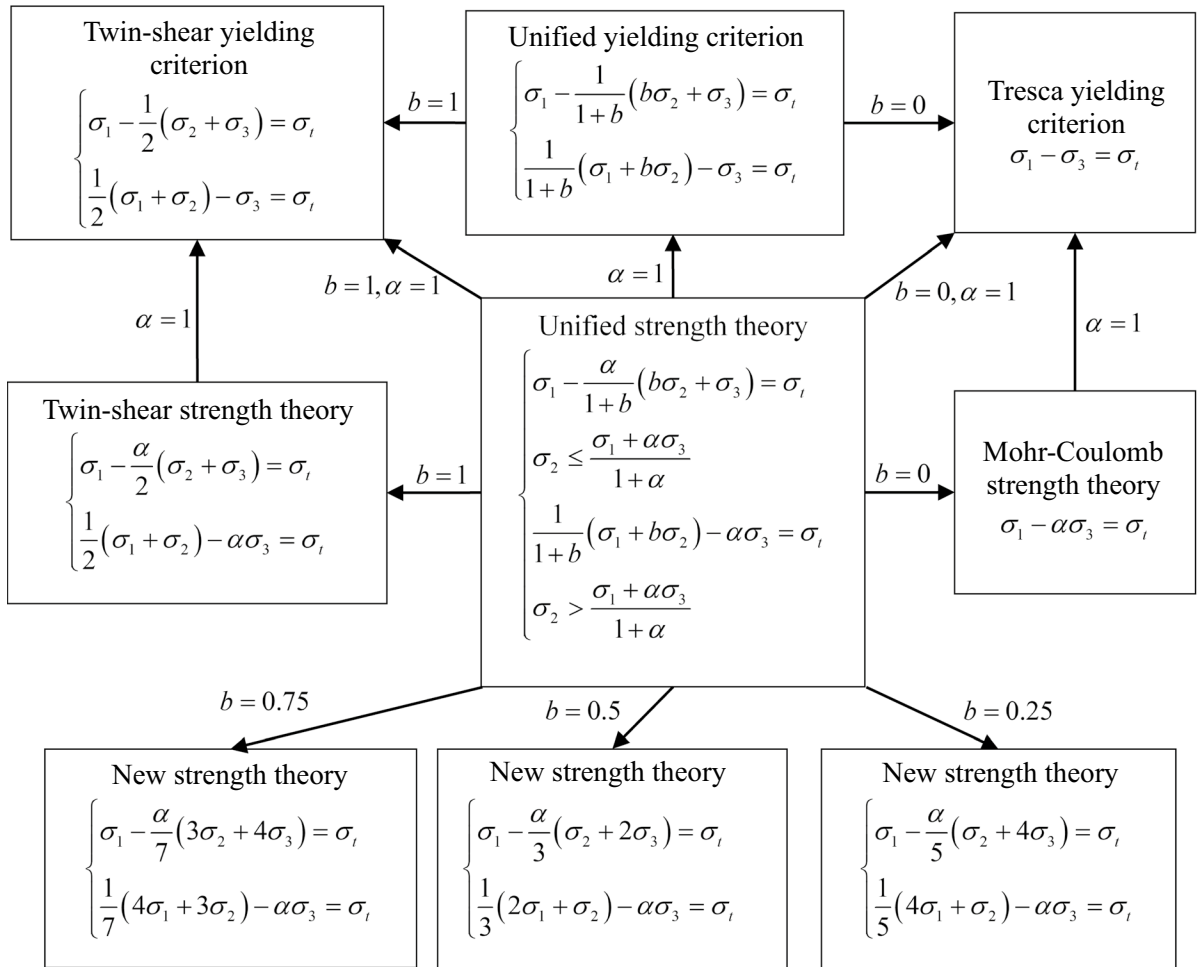
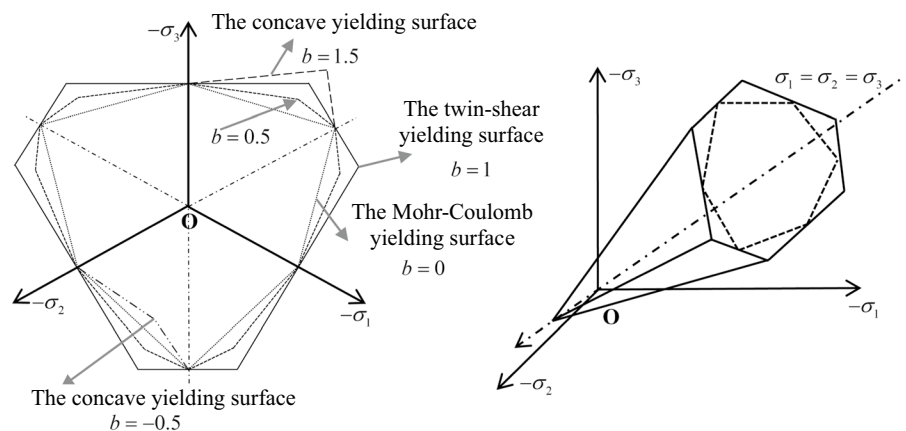


Fig. 4 The unified strength theory and its special cases

Fig. 5 The yielding surface of the unified strength theory in the π -plane and the principal stress space



In recent years, experimental studies on the failure properties of materials under complex stress states have shown that the plastic yielding surface of materials in the principal stress space has the following characteristics (Yu et al. 2000, 2006, 2009; Yu 2004, 2018; Yu and Li 2012):

1. In the compressive stress region, the trace of the yielding surface in the π -plane is a convex and non-circular smooth curve.
2. Under low compression stress, the trace of the yielding surface in the π -plane is approximately a triangle. When the compression stress increases continuously, it becomes a three-petal curve, which is close to a circle.
3. In the meridian plane, the trace of the yielding surface is convex and smooth, and the plastic yielding surface expands as the increase of compression stress.
4. The tensile strength and the compressive strength of materials are different, and the equal biaxial compression strength is not equal to the uniaxial compressive strength. The general strength theory should include more material parameters.

Based on the above experimental phenomenon, Yu et al. (2000, 2004) added the following nonlinear mathematical expression of the hydrostatic stress into the plastic yielding function of the unified strength theory to distinguish the uniaxial compression strength and the equal biaxial compression strength:

$$\begin{cases} \tau_{13} + \beta\sigma_{13} + b(\tau_{12} + \beta\sigma_{12}) + A\sigma_m + B\sigma_m^2 = C, & \tau_{12} + \beta\sigma_{12} \geq \tau_{23} + \beta\sigma_{23} \\ \tau_{13} + \beta\sigma_{13} + b(\tau_{23} + \beta\sigma_{23}) + A\sigma_m + B\sigma_m^2 = C, & \tau_{12} + \beta\sigma_{12} < \tau_{23} + \beta\sigma_{23} \end{cases} \quad (8)$$

where A , B , and C are the undetermined material parameters.

Under certain complex stress states, the strength of the material is higher than the expected value given by the single-shear strength theory. Furthermore, increasing or decreasing the value of the intermediate principal stress will cause rock failure. The unified strength theory appropriately establishes the mathematical expression for the piecewise effect of intermediate principal stress on the material strength. The unified strength theory remarkably

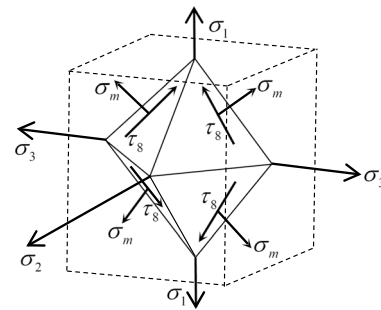


Fig. 6 Isoclinal octahedron stress model

resolves these influences of intermediate principal stress on the strength of the material. Besides, it contains various strength theories, and its yielding surface includes the convex and concave types. Therefore, it can be applied to a wider range of materials. Using the unified strength theory can further develop the material potential and improve the economic benefits of the material strength design.

2.3 Triple-shear strength theories

The triple-shear strength theories refer to the shear strength theories that take the maximum shear stress, intermediate shear stress, minimum shear stress, and corresponding normal stresses as the material plastic yielding criterion.

In 1913, Mises proposed the shear deformation energy theory, and the shear deformation energy of the stress element is identified as the material plastic yielding criterion. Mises theory is applicable to conventional metal materials with equal tensile and compressive strength. Generally, the hydrostatic stress does not affect its shear strength. Therefore, the normal stress σ_m at the isoclinal octahedron element is ignored in its plastic yielding criterion. Besides, for linear elastic materials, the shear deformation energy is proportional to the square of the

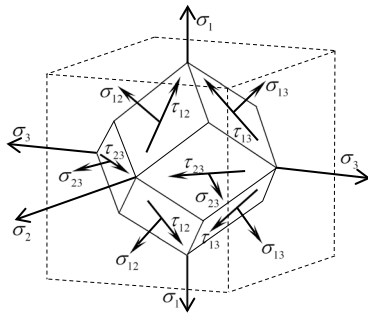


Fig. 7 Dodecahedron stress model (triple-shear stress model)

shear stress τ_8 on the isoclinal octahedron element (see Fig. 6).

In order to consider the influence of hydrostatic stress on plastic yield and clarify the difference between tensile strength and compressive strength, Drucker and Prager made the following improvements to the Mises shear deformation energy theory of geotechnical materials (Shen 1995):

$$\left(\sigma_8 = \sigma_m, \tau_8 = \frac{2}{3} \sqrt{\tau_{13}^2 + \tau_{12}^2 + \tau_{23}^2} \right)$$

$$\tau_8 + A\sigma_8 = C \tag{9}$$

where A and C are the undetermined material parameters. However, Drucker–Prager’s theory does not consider the influence of the spatial stress angle θ on the strength of the material, and the traces of its yielding surface in all meridian planes are identical, which contradicts the actual strength experimental results (Yu et al. 2000, 2004).

For this reason, Zienkiewicz and Pande (1977) recommended the following general modified model to reflect the influence of the stress angle θ on the strength of the material:

$$\left(\sqrt{J_2} / g(\theta) \right)^2 + A\sigma_m + B\sigma_m^2 = C \tag{10}$$

where A , B , and C are the undetermined material parameters. Similarly, based on analyzing the unified

$$\begin{cases} (1 - \gamma)[(\tau_{13} + \beta\sigma_{13}) + b(\tau_{12} + \beta\sigma_{12})] + \gamma(\tau_8 + \beta\sigma_8) + A\sigma_m + B\sigma_m^2 = C, & \tau_{12} + \beta\sigma_{12} \geq \tau_{23} + \beta\sigma_{23} \\ (1 - \gamma)[(\tau_{13} + \beta\sigma_{13}) + b(\tau_{23} + \beta\sigma_{23})] + \gamma(\tau_8 + \beta\sigma_8) + A\sigma_m + B\sigma_m^2 = C, & \tau_{12} + \beta\sigma_{12} < \tau_{23} + \beta\sigma_{23} \end{cases} \tag{12}$$

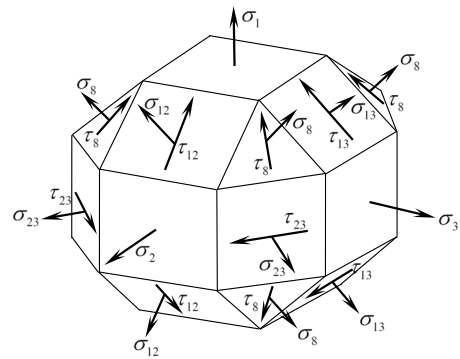


Fig. 8 Rhombicuboctahedron stress model

strength theory and the Mohr–Coulomb strength theory, Hu and Yu (2004) proposed the following triple-shear unified strength theory by using the three shear stresses on the dodecahedron (see Fig. 7) and their normal stresses on the acting plane to characterize the strength of material:

$$\begin{aligned} & (\tau_{13} + \beta\sigma_{13}) + b(\tau_{12} + \beta\sigma_{12}) \left(1 - \frac{\sigma_2 - \sigma_3}{\sigma_1 - \sigma_3} \right) \\ & + b(\tau_{23} + \beta\sigma_{23}) \frac{\sigma_2 - \sigma_3}{\sigma_1 - \sigma_3} = (1 + \beta)(1 + b)\sigma_t \end{aligned} \tag{11}$$

Similarly, Yu (2007) proposed a more generalized nonlinear unified strength theory based on the rhombicuboctahedron stress model (see Fig. 8), which unifies many commonly used linear and nonlinear strength criteria. The rhombicuboctahedron stress model has octahedral shear stress, hydrostatic stress, three principal stresses, three principal shear stresses, and corresponding normal stresses. Yu (2007) investigated the influence of these stresses on the yielding of the material, adopted the two-equations modeling method of unified strength theory, and minimized undetermined material parameters to build a mathematical expression of the plastic shear yielding function as follows (Yu et al. 2009; Yu and Li 2012):

where β is the coefficient reflecting the influence of normal stress, b is the effective coefficient of intermediate principal stress, γ is the reaction coefficient of nonlinear yielding failure, and $A, B,$ and C are the undetermined material parameters. With the help of this more generalized mathematical expression, the new nonlinear unified strength theory contains the Mohr–Coulomb criterion, the Drucker-Prager criterion, the Huber-Von Mises criterion, the unified strength criterion, and a series of new linear and nonlinear strength criteria.

Unlike the linear unified yielding criterion, the nonlinear unified yielding criterion has a nonlinear yielding surface and is applied to the nonlinear yielding behavior analysis of the material. Besides, the nonlinear unified yielding criteria overcome the multiple-slipping planes and unstable slipping plane problems in the linear unified yielding criterion (Yu 2004, 2018; Yu et al. 2006).

From the theoretical point of view, the shear strength theories can reasonably quantify the plastic shear yielding characteristics of the material. Nevertheless, they still need to be calibrated by the experiments. Based on the above shear yielding strength theories, many empirical strength criteria are developed and studied in rock mass engineering.

2.4 Empirical strength criteria

The empirical strength criterion is more consistent with the characteristics of engineering rock mass through the data provided by a large number of strength tests. The generalized Hoek–Brown criterion is the most famous criterion in the empirical strength criterion of plastic shear yield of engineering rock mass.

If the compressive stress is negative, the generalized Hoek–Brown empirical strength criterion frequently used in rock mechanics is expressed as follows (Hoek et al. 1992):

$$\sigma_3 = \sigma_1 - \sigma_{ci} [s - m_b \sigma_1 / \sigma_{ci}]^n \tag{13}$$

where $m_b, s,$ and n are rock mass parameters, and σ_{ci} is the uniaxial compressive strength of intact rock.

Furthermore, the generalized Hoek–Brown criterion and Hajiabdolmajid’s CWFS model were combined to establish the following yielding criterion to study the

mechanical characteristics of the progressively brittle failure in hard rocks (Walton et al. 2015):

$$\sigma_3 = \sigma_1(\epsilon^p) - \sigma_{ci} [s(\epsilon^p) - m_b \sigma_1(\epsilon^p) / \sigma_{ci}]^n \tag{14}$$

where $s(\epsilon^p)$ is the bonding strength, and $\sigma_1(\epsilon^p)$ is the friction strength. Both depend on the equivalent plastic strain ϵ^p . As the plastic deformation increases, the bonding strength is mobilized ahead of the friction strength, and it is continuously weakening. Meanwhile, the friction strength is mobilized and continuously strengthening. If the equivalent plastic strain exceeds ϵ_c^p , the bonding strength no longer decreases and remains stable. When the equivalent plastic strain increases and exceeds ϵ_f^p , the friction strength stays at a maximum value. This criterion can well reflect the gradual brittleness failure of hard rock and agrees with the brittleness characteristics of the engineering rock mass.

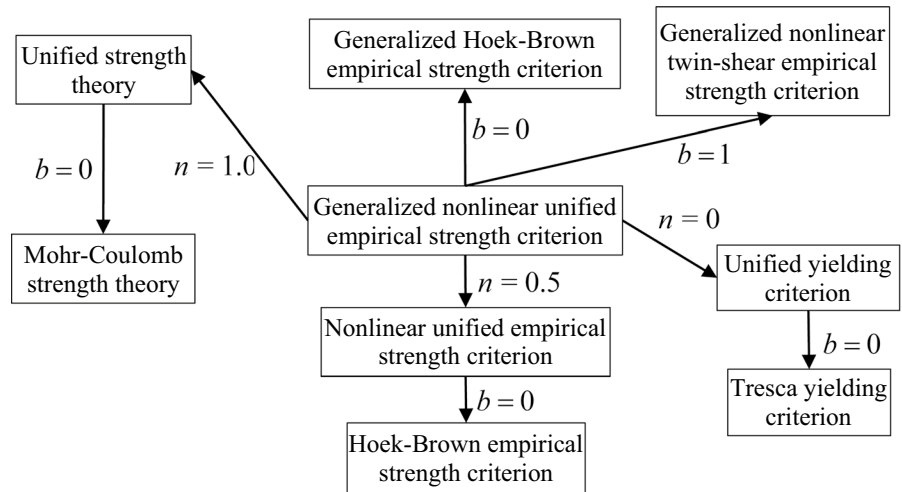
The generalized Hoek–Brown empirical strength criterion does not include the intermediate principal stress, so it cannot reflect the effect of intermediate principal stress on material strength. Thus, Singh al. (1998) revised the generalized Hoek–Brown empirical strength criterion as follows:

$$\sigma_3 = \sigma_1 - \sigma_{ci} [s - m_b(\sigma_1 + \sigma_2) / (2\sigma_{ci})]^n \tag{15}$$

This criterion reflects the effect of intermediate principal stress on the material yielding.

However, this revised generalized Hoek–Brown empirical strength criterion cannot reflect the piecewise feature of intermediate principal stress and its different impact on different materials. To reasonably reflect the piecewise effect of intermediate principal stress on the yielding of geotechnical materials, Zan and Yu (2013) introduced the double-shear stress function of the unified strength theory into the generalized Hoek–Brown empirical strength criterion. They used the two-piecewise modeling method to establish the mathematical expression of the plastic shear yielding function and proposed the generalized nonlinear unified empirical strength criterion of engineering rock mass (Yu et al. 2002; Zan et al. 2002, 2004) as follows:

Fig. 9 The generalized nonlinear unified empirical strength criterion and its exceptional cases



$$\begin{cases} F_1 = \left[\sigma_1 - \frac{1}{1+b}(b\sigma_2 + \sigma_3) \right] - \sigma_{ci} \left[s - \frac{m_b \sigma_1}{\sigma_{ci}} \right]^n = 0, & F_1 \geq F_2 \\ F_2 = \left[\frac{1}{1+b}(\sigma_1 + b\sigma_2) - \sigma_3 \right] - \sigma_{ci} \left[s - \frac{m_b(\sigma_1 + b\sigma_2)}{(1+b)\sigma_{ci}} \right]^n = 0, & F_1 < F_2 \end{cases} \quad (16)$$

If $b = 0$, the generalized nonlinear unified empirical strength criterion is degraded to the generalized Hoek–Brown empirical strength criterion (see Fig. 9) and becomes the lower bound of all external convex yielding surfaces. If $b = 1$, the generalized nonlinear unified empirical strength criterion is degraded to the generalized nonlinear twin-shear empirical strength criterion of rock mass and becomes the upper bound of all external convex yielding surfaces. Based on the Hoek–Brown empirical strength criterion, the generalized nonlinear unified empirical strength criterion can sufficiently express the essential characteristics of the strength of engineering rock mass. The generalized nonlinear unified empirical strength criterion combines the unified strength theory and the generalized Hoek–Brown empirical strength criterion to build a new system of empirical strength criteria for engineering rock mass (Yu et al. 2002; Zan et al. 2002, 2004; Zan and Yu 2013).

Using the Hoek–Brown empirical strength criterion as a development guideline for the multi-shear yielding strength criteria of engineering rock mass helps the practical application and promotion.

3 The unified strength theory and its elastic–plastic stress update algorithm

Since most finite element codes do not have a built-in constitutive algorithm related to the unified strength theory, it is necessary to develop an elastic–plastic constitutive algorithm based on the unified strength theory to simulate the strength of rock material.

Assuming that the rock material is isotropic and linearly elastic before yielding. Under the framework of small elastic deformation, the stress–strain relationship can be obtained as follows (Yu 2004, 2018; Yu et al. 2006, 2009; Yu and Li 2012):

$$\boldsymbol{\sigma} = \mathbf{C} : \boldsymbol{\varepsilon} = 2\mu dev(\boldsymbol{\varepsilon}) + Ktr(\boldsymbol{\varepsilon})\mathbf{I} \quad (17)$$

where $\boldsymbol{\sigma}$ is the Cauchy stress, $\boldsymbol{\varepsilon}$ is the elastic strain, \mathbf{C} is the elastic tangent modulus, μ is shear modulus, K is the bulk modulus, \mathbf{I} is the unit tensor, $dev(\boldsymbol{\varepsilon})$ is the deviatoric strain, and $tr(\boldsymbol{\varepsilon})$ is the trace of the elastic strain. The plastic yielding function of rock material is expressed as follows:

$$F(\boldsymbol{\sigma}, q) = F'(\boldsymbol{\sigma}) - g(q) = 0 \quad (18)$$

where q is the equivalent plastic strain.

The deformation state of a material particle at the time t_n is expressed by these variables $(\boldsymbol{\sigma}_n, \boldsymbol{\varepsilon}_n, \boldsymbol{\varepsilon}_n^e, \boldsymbol{\varepsilon}_n^p, p_n)$. $\boldsymbol{\sigma}_n$ is the Cauchy stress, $\boldsymbol{\varepsilon}_n$ is

the strain, $\boldsymbol{\epsilon}_n^p$ is the plastic strain, $\boldsymbol{\epsilon}_n^e$ is the elastic strain, and q_n is the equivalent plastic strain. In addition, the deformation state of the material particle at the time t_{n+1} , which is the succeeding time step after the time t_n , is expressed by these variables $(\boldsymbol{\sigma}_{n+1}, \boldsymbol{\epsilon}_{n+1}, \boldsymbol{\epsilon}_{n+1}^e, \boldsymbol{\epsilon}_{n+1}^p, p_{n+1})$. $\boldsymbol{\sigma}_{n+1}$ is the Cauchy stress, $\boldsymbol{\epsilon}_{n+1}$ is the strain, $\boldsymbol{\epsilon}_{n+1}^p$ is the plastic strain, $\boldsymbol{\epsilon}_{n+1}^e$ is the elastic strain, and q_{n+1} is the equivalent plastic strain. If the strain increment obtained at the next time step t_{n+1} is $d\boldsymbol{\epsilon}$, then the trial stress $\boldsymbol{\sigma}_{n+1}^{trial}$ is calculated as follows:

$$\begin{cases} \frac{\partial F}{\partial I_1} = \frac{1-\alpha}{3} \\ \frac{\partial F}{\partial \sqrt{J_2}} = \frac{2+\alpha}{\sqrt{3}} \cos \theta + \frac{\alpha(1-b)}{1+b} \sin \theta \\ \frac{\partial F}{\sqrt{J_2} \partial \theta} = \frac{\alpha(1-b)}{1+b} \cos \theta - \frac{2+\alpha}{\sqrt{3}} \sin \theta \\ \text{if } F_1 \geq F_2 \end{cases}, \begin{cases} \frac{\partial F}{\partial I_1} = \frac{1-\alpha}{3} \\ \frac{\partial F}{\partial \sqrt{J_2}} = \left(\alpha + \frac{2-b}{1+b}\right) \frac{\cos \theta}{\sqrt{3}} + \left(\alpha + \frac{b}{1+b}\right) \sin \theta \\ \frac{\partial F}{\sqrt{J_2} \partial \theta} = \left(\alpha + \frac{b}{1+b}\right) \cos \theta - \left(\alpha + \frac{2-b}{1+b}\right) \frac{\sin \theta}{\sqrt{3}} \\ \text{if } F_1 < F_2 \end{cases} \quad (21)$$

$$\boldsymbol{\sigma}_{n+1}^{trial} = \boldsymbol{\sigma}_n + \mathbf{C} : d\boldsymbol{\epsilon} \quad (19)$$

3.1 Plastic flow rule and its singularity treatments

To facilitate the numerical calculation and for the sake of simplicity, the yielding function and its partial derivative are commonly expressed by the three stress invariants as follows:

$$\begin{cases} \frac{\partial F}{\partial \boldsymbol{\sigma}} = \frac{\partial F}{\partial I_1} \frac{\partial I}{\partial \boldsymbol{\sigma}} + \frac{\partial F}{\partial \sqrt{J_2}} \frac{\partial \sqrt{J_2}}{\partial \boldsymbol{\sigma}} + \frac{\partial F}{\partial \theta} \frac{\partial \theta}{\partial \boldsymbol{\sigma}} = C_1 \mathbf{a}_1 + C_2 \mathbf{a}_2 + C_3 \mathbf{a}_3 \\ C_1 = \frac{\partial F}{\partial I_1}, \quad C_2 = \frac{\partial F}{\partial \sqrt{J_2}} + \frac{\cot 3\theta}{\sqrt{J_2}} \frac{\partial F}{\partial \theta}, \quad C_3 = -\frac{\cot 3\theta}{3J_3} \frac{\partial F}{\partial \theta} = -\frac{\sqrt{3}}{2 \sin 3\theta \sqrt{J_2^3}} \frac{\partial F}{\partial \theta} \\ \mathbf{a}_1 = [1, 1, 1, 0, 0, 0]^T \\ \mathbf{a}_2 = \frac{1}{2\sqrt{J_2}} [\sigma'_{11}, \sigma'_{22}, \sigma'_{33}, 2\tau_{12}, 2\tau_{23}, 2\tau_{13}]^T \\ \mathbf{a}_3 = \left[\sigma'_{22}\sigma'_{33} - \tau_{23}^2 + \frac{J_2}{3}, \sigma'_{11}\sigma'_{33} - \tau_{13}^2 + \frac{J_2}{3}, \sigma'_{11}\sigma'_{22} - \tau_{12}^2 + \frac{J_2}{3}, 2(\tau_{23}\tau_{13} - \sigma'_{33}\tau_{12}), \right. \\ \left. 2(\tau_{12}\tau_{13} - \sigma'_{11}\tau_{23}), 2(\tau_{12}\tau_{23} - \sigma'_{22}\tau_{13}) \right]^T \end{cases} \quad (20)$$

According to the associated plastic flow rule, the partial derivative of the yielding function is the plastic flow vector obtained at the yielding point. By substituting the three variables (C_1, C_2, C_3) and the stress state at the yielding point into Eq. (20) to obtain the plastic flow vector $\partial F / \partial \boldsymbol{\sigma}$.

According to Eq. (20) and the unified strength theory, substituting the partial derivative of (F_1, F_2) and the three stress invariants $(I_1, \sqrt{J_2}, \theta)$ into Eq. (7), and the following equations are applied to calculate the plastic flow vector obtained at the yielding point:

As shown in Fig. 10, the unified strength theory has two singularity regions at the two cross-regions of its two yielding surfaces with the two axes and one singularity region inside the two axes at the cross-region between its two yielding surfaces.

For the unified strength theory, if any of the following conditions are met: $\theta = 0^\circ$, $\theta = 60^\circ$, $F_1 = F_2$, it means that the yielding point is located in any of the three singular regions and the plastic flow vector obtained at these yielding points is singular.

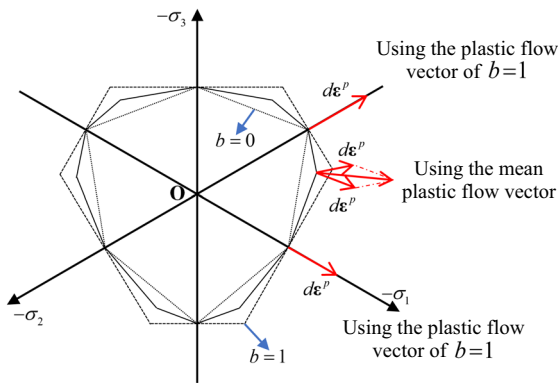


Fig. 10 Treating the singular plastic flow vectors in unified strength theory

Therefore, the following methods are used to calculate the plastic flow vectors at the three singular regions (see Fig. 10):

1. If conditions $F_1 = F_2$ and $\theta = \theta_b$ are satisfied, then the yielding point is located in the singular region, and the mean plastic flow vector is taken. By summing the plastic flow vectors of the two yielding functions, the mean plastic flow vector is obtained as follows:

$$\begin{cases} C_1 = \left(\lim_{\theta \rightarrow \theta_b^+} C_1 + \lim_{\theta \rightarrow \theta_b^-} C_1 \right) / 2 \\ C_2 = \left(\lim_{\theta \rightarrow \theta_b^+} C_2 + \lim_{\theta \rightarrow \theta_b^-} C_2 \right) / 2 \\ C_3 = \left(\lim_{\theta \rightarrow \theta_b^+} C_3 + \lim_{\theta \rightarrow \theta_b^-} C_3 \right) / 2 \end{cases} \quad (22)$$

2. If the yielding point is located in any one of the two singular regions satisfying the condition $\theta = 0^\circ$ or $\theta = 60^\circ$, then the plastic flow vector is obtained by using the double-shear parameter $b = 1$. The plastic flow vector adapted to correct the singular plastic flow vector in the programming is as follows:

$$\begin{cases} C_1 = C_1 = \frac{1-\alpha}{3} \\ C_2 = C_2 = \frac{2}{3\sqrt{3}}(2+\alpha) \\ C_3 = C_3 = \frac{(2+\alpha)}{6J_2} \\ \theta = 0^\circ \end{cases}, \quad \begin{cases} C_1 = C_1 = \frac{1-\alpha}{3} \\ C_2 = C_2 = \frac{2}{3\sqrt{3}}(1+2\alpha) \\ C_3 = C_3 = -\frac{(1+2\alpha)}{6J_2} \\ \theta = 60^\circ \end{cases} \quad (23)$$

3.2 Elastic–plastic stress update algorithm

3.2.1 Explicit forward integral algorithm

At first, substituting the trial stress into the yielding function to obtain the loading criteria:

$$\begin{cases} F(\sigma_{n+1}^{trial}, q_n) \leq 0, \text{ elastic loading} \\ F(\sigma_{n+1}^{trial}, q_n) > 0, \text{ plastic loading} \end{cases} \quad (24)$$

If $F(\sigma_{n+1}^{trial}, q_n) \leq 0$, the current stress is directly updated to the test stress without any plastic yielding during this process. Moreover, the plastic strain increment and the equivalent plastic strain increment are zero, and the continuous tangent modulus equals the elastic modulus C .

If $F(\sigma_{n+1}^{trial}, q_n) > 0$, the material particle has plastic deformation. The stress σ_{n+1}^0 at the initial yielding point is first solved by the following equations:

$$\begin{cases} \sigma_{n+1}^0 = \sigma_n + \eta C : d\epsilon, \quad 0 \leq \eta \leq 1 \\ q_{n+1}^0 = q_n, \quad F(\sigma_{n+1}^0, q_{n+1}^0) = 0 \\ d\epsilon^m = (1 - \eta)d\epsilon / m \end{cases} \quad (25)$$

The remaining strain increment $(1 - \eta)d\epsilon$ is divided into m equal parts. For each equal strain increment $d\epsilon^m$, the associated flow rule and an explicit forward integral algorithm are used to update the stress and state variables. The calculation scheme at step i is as follows (see Fig. 11):

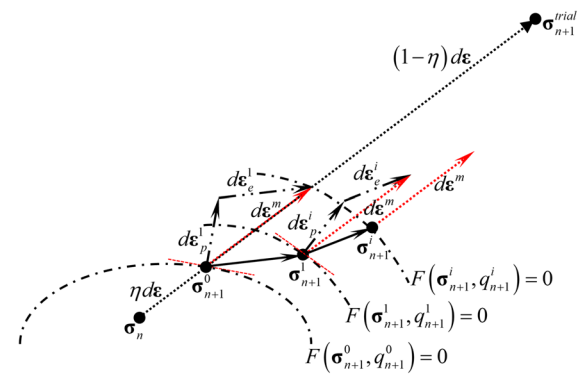


Fig. 11 Schematic diagram of the explicit forward integral algorithm

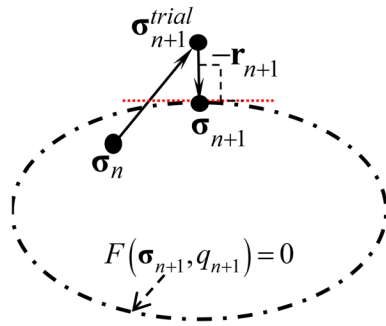


Fig. 12 Implicit return mapping algorithm under associated flow rule

$$\begin{cases} i = 1, \dots, m, \quad \mathbf{r}_{n+1}^i = \left(\frac{\partial F}{\partial \boldsymbol{\sigma}_{n+1}^{i-1}} \right) / \left\| \frac{\partial F}{\partial \boldsymbol{\sigma}_{n+1}^{i-1}} \right\| \\ \Delta \lambda = \frac{\mathbf{r}_{n+1}^i : (\mathbf{C} : d\boldsymbol{\varepsilon}^m)}{\mathbf{r}_{n+1}^i : \mathbf{C} : \mathbf{r}_{n+1}^i - \sqrt{2/3} (\partial F / \partial q_{n+1}^{i-1}) / \left\| \frac{\partial F}{\partial \boldsymbol{\sigma}_{n+1}^{i-1}} \right\|} \\ q_{n+1}^i = q_{n+1}^{i-1} + \sqrt{2/3} \Delta \lambda, \quad d\boldsymbol{\varepsilon}_p^i = \Delta \lambda \mathbf{r}_{n+1}^i, \quad d\boldsymbol{\varepsilon}_e^i = d\boldsymbol{\varepsilon}^m - d\boldsymbol{\varepsilon}_p^i \\ \boldsymbol{\sigma}_{n+1}^i = \boldsymbol{\sigma}_{n+1}^{i-1} + \mathbf{C} : d\boldsymbol{\varepsilon}_e^i = \boldsymbol{\sigma}_{n+1}^{i-1} + \mathbf{C}_{ep}^i : d\boldsymbol{\varepsilon}^m \\ \mathbf{C}_{ep}^i = \left[\mathbf{C} - \frac{(\mathbf{C} : \mathbf{r}_{n+1}^i) \otimes (\mathbf{r}_{n+1}^i : \mathbf{C})}{\mathbf{r}_{n+1}^i : \mathbf{C} : \mathbf{r}_{n+1}^i - \sqrt{2/3} (\partial F / \partial q_{n+1}^{i-1}) / \left\| \frac{\partial F}{\partial \boldsymbol{\sigma}_{n+1}^{i-1}} \right\|} \right] \end{cases} \quad (26)$$

Furthermore, the final stress state and its associated plastic flow vector are taken into the last expression of Eq. (26) to obtain the continuous tangent modulus \mathbf{C}_{ep}^m . By substituting $\partial F / \partial q = 0$ into the above expression, the stress update scheme and the continuous tangent modulus for the ideal plastic materials with the associated plastic flow rule are obtained.

In the explicit forward integral algorithm, the stress will deviate from the yielding surface, resulting in the last updated stress point outside the yielding surface, and its continuous tangent modulus will decrease convergence speed. It is easy to result in a non-converging calculation. Unlike the explicit forward integral algorithm introduced earlier, the implicit return mapping algorithm and semi-implicit return mapping algorithm do not cause the stress to deviate from the yielding surface. Moreover, they calculate faster than

the explicit forward integral algorithm and belong to the unconditional convergence algorithm.

3.2.2 Implicit return mapping algorithm

The plastic flow vector of the fully implicit method is the normal vector of the final yielding point $\boldsymbol{\sigma}_{n+1}$, which is unknown during the solution. In the fully implicit method, the trial stress returns to the updated yielding surface $F(\boldsymbol{\sigma}_{n+1}, q_{n+1}) = 0$ along the plastic flow vector of the stress point $\boldsymbol{\sigma}_{n+1}$. The plastic strain increment is $\Delta \lambda \mathbf{r}_{n+1} = \Delta \lambda (\partial F / \partial \boldsymbol{\sigma}_{n+1}) / \left\| (\partial F / \partial \boldsymbol{\sigma}_{n+1}) \right\|$, and the equivalent plastic strain increment is $\sqrt{2/3} \Delta \lambda$. By applying the constraint condition $\left\| \partial F / \partial \boldsymbol{\sigma}_{n+1} \right\| = 1$ to the yielding function, the following equations can be obtained (see Fig. 12):

$$\begin{cases} \boldsymbol{\sigma}_{n+1} = \boldsymbol{\sigma}_{n+1}^{trial} - \mathbf{C} : \Delta \lambda (\partial F / \partial \boldsymbol{\sigma}_{n+1}) \\ \boldsymbol{\varepsilon}_{n+1}^p = \boldsymbol{\varepsilon}_n^p + \Delta \lambda (\partial F / \partial \boldsymbol{\sigma}_{n+1}) \\ q_{n+1} = q_n + \sqrt{2/3} \Delta \lambda, \quad F(\boldsymbol{\sigma}_{n+1}, q_{n+1}) = 0 \end{cases} \quad (27)$$

The consistent tangent modulus of the implicit return mapping algorithm can be expressed as follows:

$$\begin{cases} \mathbf{C}_{ep}^{ctm} = \boldsymbol{\Xi} - \frac{[\boldsymbol{\Xi} : (\partial F / \partial \boldsymbol{\sigma}_{n+1})] \otimes [(\partial F / \partial \boldsymbol{\sigma}_{n+1}) : \boldsymbol{\Xi}]}{(\partial F / \partial \boldsymbol{\sigma}_{n+1}) : \boldsymbol{\Xi} : (\partial F / \partial \boldsymbol{\sigma}_{n+1}) - \sqrt{2/3} (\partial F / \partial q_{n+1})} \\ \boldsymbol{\Xi} = [\mathbf{C}^{-1} + \Delta \lambda (\partial^2 F / \partial \boldsymbol{\sigma}_{n+1}^2)]^{-1} \end{cases} \quad (28)$$

Since the partial derivatives of the plastic flow vector at the terminal stress point need to be solved, the fully implicit method requires numerous calculations and is very complicated. Due to the local singularities in the first-order partial derivatives of the non-smooth piecewise linear yielding function, solving its second-order partial derivatives is a very challenging problem. Besides, calculating the consistent tangent modulus in the fully implicit algorithm is very intricate. Therefore, this study does not use the fully implicit algorithm to update the stress state and the consistent tangent modulus.

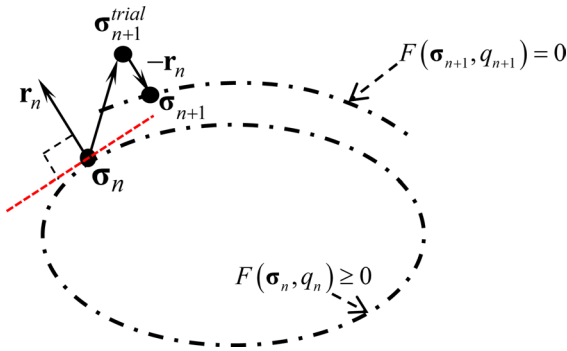


Fig. 13 Semi-implicit return mapping algorithm under associated flow rule

3.2.3 Semi-implicit return mapping algorithm

Unlike the fully implicit method, the plastic flow vector of the semi-implicit return mapping algorithm is known during the solution. In the semi-implicit algorithm, the plastic flow vector of the stress point σ_n at the time t_n should be first calculated as $r_n = (\partial F / \partial \sigma_n) / \|(\partial F / \partial \sigma_n)\|$. By return-

ing from the trial stress point σ_{n+1}^{trial} along the plastic flow vector r_n to the updated yielding surface $F(\sigma_{n+1}, q_{n+1}) = 0$ at the time t_{n+1} . The stress σ_{n+1} , the plastic strain increment $\Delta \lambda r_n$, and the equivalent plastic strain increment $\sqrt{2/3} \Delta \lambda$ are obtained as follows (see Fig. 13):

$$\begin{cases} \sigma_{n+1} = \sigma_{n+1}^{trial} - C : \Delta \lambda r_n, & \epsilon_{n+1}^p = \epsilon_n^p + \Delta \lambda r_n \\ q_{n+1} = q_n + \sqrt{2/3} \Delta \lambda, & F(\sigma_{n+1}, q_{n+1}) = 0 \end{cases} \quad (29)$$

By simplifying Eq. (29), the univariate function $f(\Delta \lambda)$ can be obtained as follows:

$$f(\Delta \lambda) = F(\sigma_{n+1}^{trial} - C : \Delta \lambda r_n, q_n + \sqrt{2/3} \Delta \lambda) = 0 \quad (30)$$

Due to the piecewise-linear and non-smooth yielding function $f(\Delta \lambda)$, the unified strength theory's derivative is singular. Accordingly, a new method without calculating the derivatives of the yielding function is required, and we propose the Aitken accelerated iteration scheme to solve the piecewise-linear and non-smooth yielding function $f(\Delta \lambda)$. With the Aitken accelerated iteration

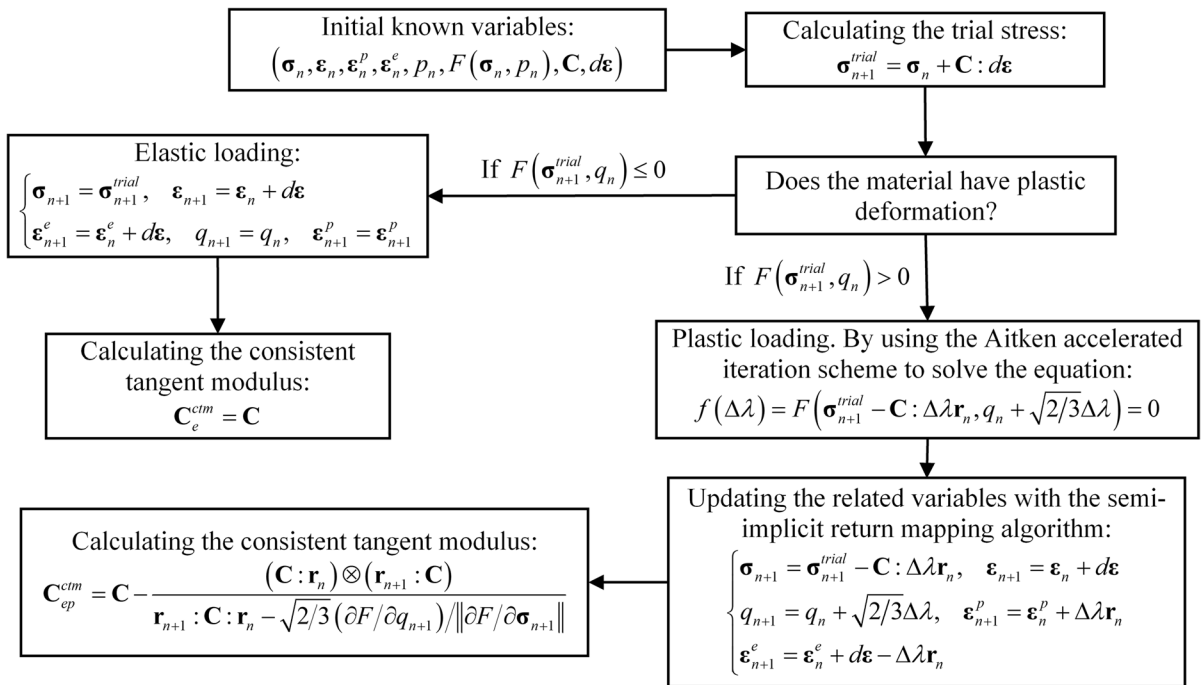


Fig. 14 The flowchart of updating stress and calculating the consistent tangent modulus

scheme, the solution is straightforward without any derivatives. Moreover, the Aitken accelerated iteration scheme can reach a second-order convergence speed.

The Aitken accelerated iteration scheme is used to solve the nonlinear equation $f(\Delta\lambda)/\omega = 0$. Where ω is used to unify the function $f(\Delta\lambda)$ and ensures that the equation value is in the same order of magnitude as $\Delta\lambda$. Furthermore, $\omega = f(\Delta\lambda = 0) / ((\mathbf{C}^{-1} : (\boldsymbol{\sigma}_{n+1}^{trial} - \boldsymbol{\sigma}_n)) : \mathbf{r}_n)$. The formula of the Aitken accelerated iteration scheme is as follows:

$$\Delta\lambda_{k+1} = \Delta\lambda_k + \frac{f(\Delta\lambda_k)^2 / \omega}{f(\Delta\lambda_k) - f[\Delta\lambda_k + f(\Delta\lambda_k) / \omega]} \quad (31)$$

The iterative solution is carried out with Eq. (31) until the constraint inequation $|f(\Delta\lambda_{k+1}) / \omega| \leq 0.1^{6\sim 8}$ can be satisfied. Substituting the $\Delta\lambda$ into Eq. (29) for updating stress, plastic strain, and equivalent plastic strain. The consistent tangent modulus of the semi-implicit return mapping algorithm is expressed as follows:

$$\mathbf{C}_{ep}^{ctm} = \mathbf{C} - \frac{(\mathbf{C} : \mathbf{r}_n) \otimes (\mathbf{r}_{n+1} : \mathbf{C})}{\mathbf{r}_{n+1} : \mathbf{C} : \mathbf{r}_n - \sqrt{2/3}(\partial F / \partial q_{n+1}) / \|\partial F / \partial \boldsymbol{\sigma}_{n+1}\|} \quad (32)$$

The semi-implicit return mapping algorithm is simpler and more efficient than the implicit return mapping algorithm. This method avoids the complexity of solving the second partial derivatives in the implicit algorithm. The semi-implicit method does not cause the issue that the stress deviates from the yielding surface. The algorithm uses the consistent tangent modulus, has second-order convergence speed, and belongs to the unconditionally convergent algorithm. It should be noted that the consistent tangent modulus of the semi-implicit return mapping algorithm is unsymmetrical, and thus, the finite element analysis will adopt an unsymmetrical solver. Figure 14 shows the flow-chart of updating stress and calculating the consistent tangent modulus by the semi-implicit return mapping algorithm and the Aitken accelerated iteration scheme.

4 Numerical verification

4.1 Theoretical analyses

A constitutive algorithm for isotropic softening plastic materials based on the unified strength theory is embedded into the finite element simulation technique. The combination method of the semi-implicit return mapping algorithm and the Aitken accelerated iteration scheme is used to update the stress and calculate the consistent tangent modulus. The self-developed material constitutive algorithm simulates an example of tunnel excavation (see Fig. 15), and the calculated results are compared with the theoretical values to verify the correctness of the self-developed constitutive algorithm. Given a circular tunnel, its radius is $a = 5$ m, the radius of its surrounding rock is $R = 30$ m, the initial pressure is $q' = 50$ MPa, and the supporting pressure is $p = 0$. The surrounding rock's elastic modulus is $E = 200$ GPa, Poisson's ratio is $\nu = 0.45$, internal friction angle is $\varphi = 45^\circ$, and cohesion strength is $c = 3$ MPa.

Assuming that the model is under plane strain state and $q' > p$, and the initial ground stress field is obtained by uniformly distributed compressive stress outside the model before it is excavated, the theoretical solution of the stress in the plastic deformation zone can be obtained by using the unified strength theory and the non-associated Mohr–Coulomb plastic flow rule (Yu 2004, 2018; Yu et al. 2006, 2009; Zeng et al. 2011; Yu and Li 2012). The mathematical formulas are derived as follows:

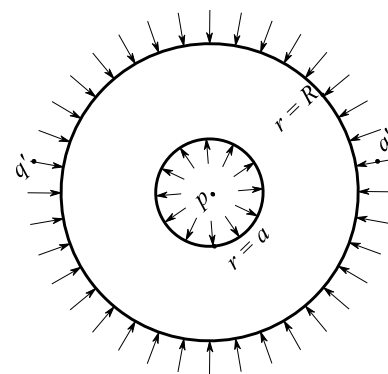


Fig. 15 Tunnel analysis model

$$\begin{cases} \sigma_r = -\left(\frac{a}{r}\right)^\eta \left(\frac{\xi}{\eta} + p\right) + \frac{\xi}{\eta} \\ \sigma_\theta = -\left(\frac{a}{r}\right)^\eta \left(\frac{\xi}{\eta} + p\right)(1 - \eta) + \frac{\xi}{\eta} \\ \xi = -\frac{(1+b)\sigma_r}{(1+b\nu)\alpha}, \quad \eta = \frac{(\alpha-1)+(2\alpha\nu-1)b}{(1+b\nu)\alpha} \end{cases} \quad (33)$$

where σ_r is the radial stress, σ_θ is the circumferential stress, and b is the double-shear parameter.

If the area of the surrounding rock is boundless, the following equations can be obtained:

$$\begin{cases} R_p \approx a \left[\frac{(\rho\eta + \xi)(2 - \eta)}{2(q'\eta + \xi)} \right]^{\frac{1}{\eta}} \\ \sigma_{R_p} = \left(\frac{a}{R_p}\right)^\eta \left(\frac{\xi}{\eta} + p\right) - \frac{\xi}{\eta} \end{cases} \quad (34)$$

where R_p is the external radius of the plastic deformation zone, and σ_{R_p} is the radial stress at the external radius of the plastic deformation zone.

If the area of the surrounding rock is finite, then the stresses in the elastic deformation zone are derived as follows:

$$\begin{cases} \sigma_r = \frac{k^2(\sigma_{R_p} - q')}{1 - k^2} - \left(\frac{R_p}{r}\right)^2 \frac{(\sigma_{R_p} - q')}{1 - k^2} - q' \\ \sigma_\theta = \frac{k^2(\sigma_{R_p} - q')}{1 - k^2} + \left(\frac{R_p}{r}\right)^2 \frac{(\sigma_{R_p} - q')}{1 - k^2} - q' \end{cases} \quad (35)$$

where $k = R_p/R$.

If the area of the surrounding rock is finite, then the radial displacement u_r in the elastic deformation zone is calculated as follows:

$$\begin{cases} u_r = \frac{(1+\nu)(\sigma_{R_p} - q')}{E(1 - k^2)} \left[k^2 r(1 - 2\nu) + \frac{R_p^2}{r} \right] \\ u_{R_p} = \frac{(1+\nu)R_p(\sigma_{R_p} - q')}{E(1 - k^2)} [k^2(1 - 2\nu) + 1] \end{cases} \quad (36)$$

where u_{R_p} is the radial displacement at the external radius of the plastic deformation zone.

The radial displacement u_r in the plastic deformation zone is calculated as follows:

$$\begin{cases} u_r = Cr^{-\frac{1}{\alpha_\psi}} + Br + Ar^{1-\eta} \\ A = -\frac{a^\eta(1+\nu)(\rho\eta + \xi)[- \eta - (2 - \eta)\nu(1 + \alpha_\psi) + \alpha_\psi + 1]}{\eta E(-\alpha_\psi \eta + \alpha_\psi + 1)} \\ B = \frac{(\nu + 1)(q'\eta + \xi)(1 - 2\nu)}{\eta E} \\ C = \left(-AR_p^{1-\eta} - BR_p + u_{R_p}\right)R_p^{1/\alpha_\psi} \end{cases} \quad (37)$$

where α_ψ is the dilatancy angle of the non-associated Mohr–Coulomb plastic flow rule. If $b = 0$ and $\alpha_\psi = \alpha$, then the Mohr–Coulomb strength theory with the associated plastic flow rule is obtained.

4.2 Numerical verifications

The stress field of tunnel excavation is simulated with the axisymmetric plane element. The region adopted in the simulation is at least three times larger than the tunnel. Its length and width are 20 m and 30 m, respectively. The model’s upper and lower boundaries apply symmetrical displacement constraints (see Fig. 16), and uniform compression stress at the external boundary is 50 MPa. First, the initial stress field is solved. Then the tunnel is excavated by using the element birth–death technique. Finally, the stress distribution of the tunnel after excavation is simulated. The tunnel model is divided into 9,221 nodes and 3,000 cells.

Figure 17 manifests the stress and displacement distributions in the disturbed excavation region and compares the finite element simulation and the theoretical analysis. In the comparative analysis of numerical experiments, the maximum relative error of radial stress is 1.569%, and its average relative error is 0.681%. The maximum relative error of circumferential stress is 2.400%, and its average relative error is 0.501%. The maximum relative error of radial displacement is 0.601%, and its average relative error is 0.387%. The plastic deformation zone

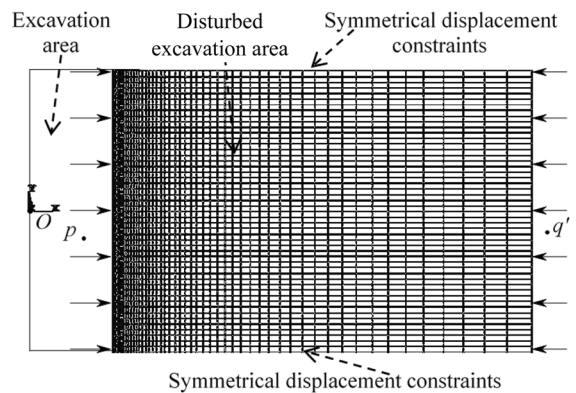


Fig. 16 The meshing and boundary conditions of the tunnel model

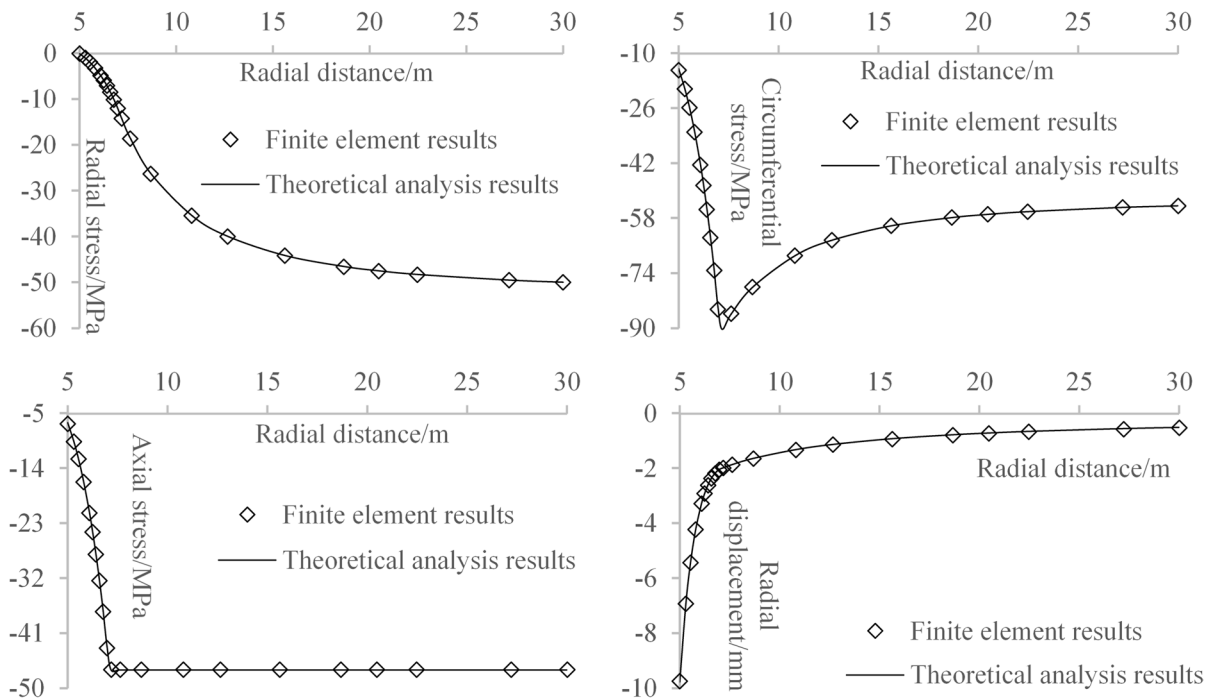


Fig. 17 Comparison between the results of finite element simulation and analytical analysis

radius of the finite element simulation solution is 7.035 m, and the corresponding theoretical analysis solution is 7.028 m, with a relative error of 0.101%. The predicted and theoretical values of the radial stress at the elastic–plastic interface are 12.748 MPa and 12.523 MPa, respectively. Moreover, their relative error is 1.797%. The numerical and theoretical values of the radial displacement at the elastic–plastic interface are -2.030 mm and -2.031 mm, respectively. Furthermore, their relative error is 0.049%. The numerical and theoretical values of the radial displacement at the excavated surface are -9.745 mm and -9.774 mm, respectively. Besides, their relative error is 0.296%.

In this study, the elastic–plastic theoretical solutions in the deep-lying circular tunnel are derived based on the condition that the surrounding rock is boundless. However, the surrounding rock is finite in the numerical simulation. Besides, the finite elements only approximately meet the plane strain state in the numerical simulation, and the accuracy of the numerical simulation is related to the mesh-division density. Therefore, there is an inevitable error between the numerical and theoretical

solutions. The simulation results show that the error between the numerical and theoretical solutions is small and meets the engineering precision requirement. The result indicates that the plastic constitutive algorithm for isotropic softening materials based on the unified strength theory is valid.

5 Engineering application: underground stope stability analysis

5.1 Engineering backgrounds

Bainiuchang Mine is a deep underground metal mine in Mengzi County, Yunnan Province, China. Its orebody in the Baiyang section is a gently inclined broken thin vein with poor mining conditions, broken rock mass, and lack of continuity. At present, the room-pillar method is used for mining. The stability of the surrounding underground rock is poor, and the stope has a serious roof caving problem. Hence, it is necessary to study the stability of the test stope in the Baiyang mine section

to improve the mining efficiency and ensure mining safety. By analyzing the stress, strain, and displacement distribution in the typical roof and pillar, the structural parameters of the test stope are hopefully optimized to instruct the mine design and safety production. The main factors of stope stability analysis are mining depth, pillar width, rock strength and room width. Among them, the first factor and the third factor are the geological engineering conditions of the stope, so only reasonable optimization of the size of pillars and rooms can improve the overall stability of the stope. Moreover, the pillar width must be bigger than 3.5 m, and the room width must be smaller than 5 m to ensure the allowable safety factor of the pillar is not less than 1.5.

5.2 Stope simulation conditions and parameters

5.2.1 Overview of orebody characteristics and mining method

The orebody of the Baiyang mine section is mainly a gently inclined thin orebody. The thickness is between 2 and 5 m. The length of the stope is about 40 m, and its width is about 25 m. Many pillars are preserved to support its roof, the pillar width is about 3 m, and the room width varies from 2 to 6 m. Because of the poor stability of rock mass, many mined stopes have been closed because of the roof caving and rock strata collapse.

5.2.2 Mechanical parameters of the engineering rock mass

The rocks related to the stope stability analysis are mainly siltstone, mudstone, carbonaceous limestone and orebody. Among them, mudstone and siltstone

are distributed in the roof, and carbonaceous limestone is distributed in the floor. The main mechanical parameters of these rock masses are listed in Table 1:

5.2.3 The initial ground stress field of the stope

The vertical ground stress of the Baiyang mine section is mainly the overburden gravity stress. According to the average ratio of Baiyang average horizontal ground stress to vertical ground stress, the horizontal ground stress field is obtained. And the average ratio is expressed as follows (Zhao et al. 2007; Jing et al. 2011):

$$k = 1.0 + (124/H) \quad (38)$$

where H is the buried depth. The average buried depth of the Baiyang mine section is $H = 500\text{m}$, so the mean ratio is $k \approx 1.25$.

5.3 The stope stability analyses

5.3.1 Numerical model

The self-developed constitutive algorithm for isotropic softening plastic materials based on the unified strength theory is used to simulate the excavation of the stope using the finite element technique. Furthermore, the distribution of the three principal stresses and the plastic yielding in the stope are analyzed. The geological model should be consistent with the actual geological conditions as much as possible, and its physical dimensions should be at least three times larger than the excavation space diameter. According to the actual engineering geology and mining conditions, the geological modeling parameters are as follows: the model range is $150\text{ m} \times 100\text{ m} \times 150\text{ m}$ (length \times width \times height); the test stope in the Baiyang

Table 1 The mechanical parameter of rock mass

Rock mass	Elasticity modulus/GPa	Poisson's ratio	Double-shear parameter	Cohesion/MPa	Friction angle/ $^{\circ}$	Density/(g/cm ³)
Mudstone	4.51	0.19	0.25	1.14	17.79	2.79
Siltstone	14.88	0.27	0.25	4.08	35.97	2.64
Orebody	12.60	0.22	0.5	6.50	42.07	4.00
Carbonaceous limestone	9.37	0.25	0.5	3.47	28.38	2.74

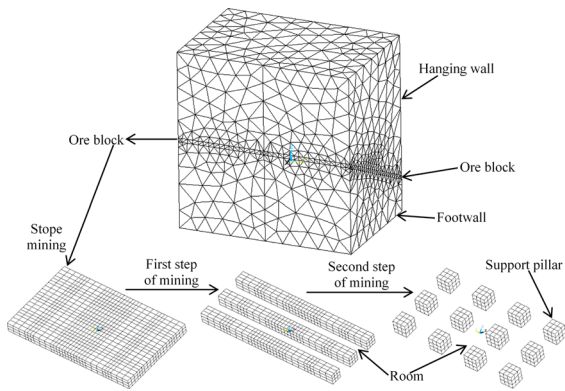


Fig. 18 The grid of the geological model and the stepwise mining diagram of the stope

mine section is about 500 m away from the surface; the orebody inclination is 25°; the orebody thickness is 3 m; the stope height is 3 m; the stope length is 40 m; the stope width is 25 m; the width of the pillar is 3 m; the row spacing interval of the pillar is 4 m; the column spacing interval of the pillar is 6 m.

When the finite element grid is divided, the stope and its local grid are refined to meet the computational accuracy, and the grid outside the stope is rough to reduce the computational workload. A simplified model of the stope is established, and then tetrahedral elements are used to divide the finite element grid for each rock mass. The entire grid is divided

into 96,866 elements and 18,513 nodes (as shown in Fig. 17). In the mining of the stope, the banded room is first excavated along the length of the block, and then the continuous pillar is excavated for the second time along the width of the block, leaving 3 m wide square pillars to support the entire stope (see Fig. 18).

The hanging wall of the stope in the model is 100 m high, and the footwall extends downward to 50 m deep. The initial ground stress field of the stope is solved according to the existing load and boundary conditions. The initial ground stress field is imported into the finite element geological model, and then the excavation of the stope is carried out. The following are the boundary and loading conditions used in the numerical model. Vertical ground stress $\sigma_v = \rho gh = 2.715 \times 9.8 \times 0.4 \text{ MPa} \approx 10.65 \text{ MPa}$ is applied to the upper surface of the model. Horizontal ground stresses $\sigma_H = 1.25 \rho gh = 16.63 \text{ MPa}$ are applied to the four outer surfaces of the model. The bottom surface of the model is constrained by a fixed boundary condition, and the acceleration of gravity is 9.8 m/s^2 .

5.3.2 Stability analysis

Because of the symmetry of this model, only half of the entire model is used for numerical simulation. When the stope is unexcavated, the initial stress field is simulated first. The maximum initial ground stress of the stope is obtained by simulation as 18.80 MPa,

Fig. 19 The maximum tensile stress and the maximum compressive stress of the stope

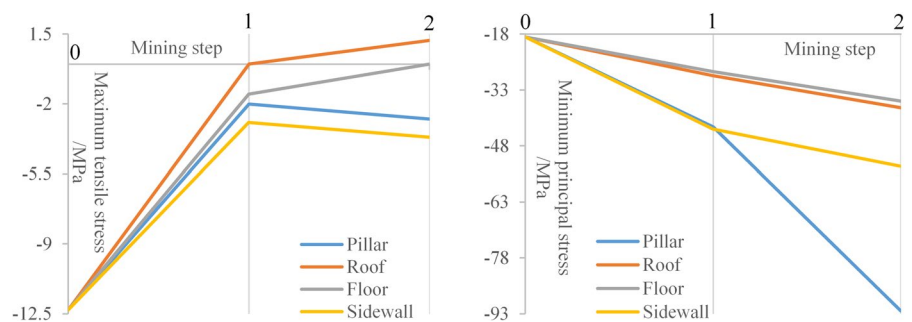
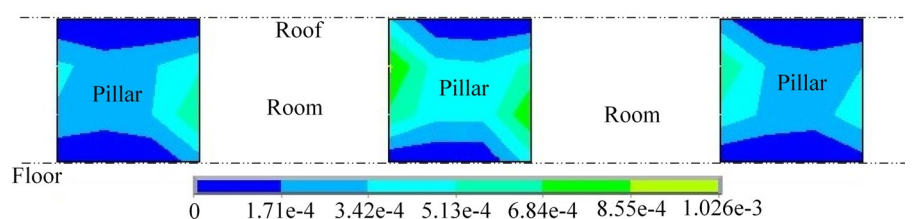


Fig. 20 The distribution of the equivalent plastic strain in the pillar



which is consistent with the actual situation. The maximum tensile stress of the roof and the maximum compressive stress of the pillar are taken as the primary criteria to determine stope stability. The stope is excavated in two steps, and the simulation results are as follows:

1. Stability analysis of the pillar.

As the excavation continues, the compressive stress in the stope increases (see Fig. 19). Moreover, the maximum compressive stress in the pillar increases five times. The compressive stress of the pillar in the middle of the stope is stronger than that of other pillars. The maximum compressive stress value 92.30 MPa appears at the bottom corner of the central pillar and quickly causes the pillar to yield locally.

Figure 20 shows the plastic deformation zone inside the pillar. The plastic deformation zones in all the pillars are widely distributed and very severe, and their equivalent plastic strains are greater than $1.710e-4$. The plastic strain of the pillar in the middle is significantly greater than the other pillars. The equivalent plastic strain runs through the entire pillar, and its value is greater than $3.420e-4$ at the midpoint. The maximum equivalent plastic strain reaches $1.026e-3$ in the waist corner of the pillar, which forms the shear failure zone and increases the possibility of the pillar peeling off.

2. Stability analysis of the roof.

Figure 21 shows the layout of potential tensile failure zone of the roof. The potential tensile failure zone is mainly concentrated in the middle of the stope, which is easy to cause roof caving.

The local maximum tensile stress of the roof is 1.18 MPa (see Fig. 19), but the average uniaxial tensile strength of the roof is less than -0.30 MPa. If the surrounding rock has many joint fissures, its tensile strength will be weakened, and even a certain compressive stress is required to maintain the stability of the rock mass. If the first principal stress in one area is greater than -0.30 MPa, then this area is taken as the potential tensile failure area. If there are too many weak structural planes in the potential tensile failure zone, the roof will collapse.

The distribution of the plastic deformation zone inside the roof is shown in Fig. 21. The roof has an extensive plastic deformation zone, and its local plastic deformation zone runs through the whole

stope. The maximum equivalent plastic strain of the roof reaches $6.902e-3$. The plastic yielding of the roof is more significant than the pillars. The plastic deformation zone is mainly concentrated near the sidewall. In the process of mining, plastic deformation occurs first in the place where the roof is close to the side wall, and then the pillar in the middle of the stope.

After the stope mining, the subsidence displacement of the roof is between 2.946 and 3.881 cm, and the subsidence displacement of the floor is between 2.750 and 3.736 cm. Naturally, under good engineering geological conditions, the subsidence displacement magnitude still can maintain the stabilization of the roof. However, the surrounding rock of Bainiuchang mine is broken and cracked, and the engineering geological condition is poor. Therefore, the settlement displacement of about 3 cm will also destabilize the stope, causing severe instability problems.

The numerical simulation results of stope stability show that the safety of the original stope is very poor, so it is necessary to optimize the structural parameters of the original stope.

5.4 Analysis of the stope instability mechanism

5.4.1 Analysis of the pillar instability mechanism

Figure 22 shows the yielding failure and compressive failure of the carbonaceous limestone pillar. The dominant failure modes of most pillars in the Baiyang mine section are shear failure and surface spalling. As the excavation continues, the pillar's compressive stress increases continuously. If the stress of the pillar is less than the rock mass strength, then the pillar remains stable. However, if the pillar's stress is greater than the ultimate bearing capacity of the rock mass, then it will be unstable.

The pillar from inside to outside can be divided into intact zone, transition zone, and crushing zone. Fragmenting failure and progressive exfoliating failure are the main failure forms of pillar in Baiyang section. They are also common failure modes of stratified orebody. The pillar is gradually damaged from the surface to the inside. At first, tensile failure appears on the pillar's surface, and then the shear failure zone develops at the pillar's corners.

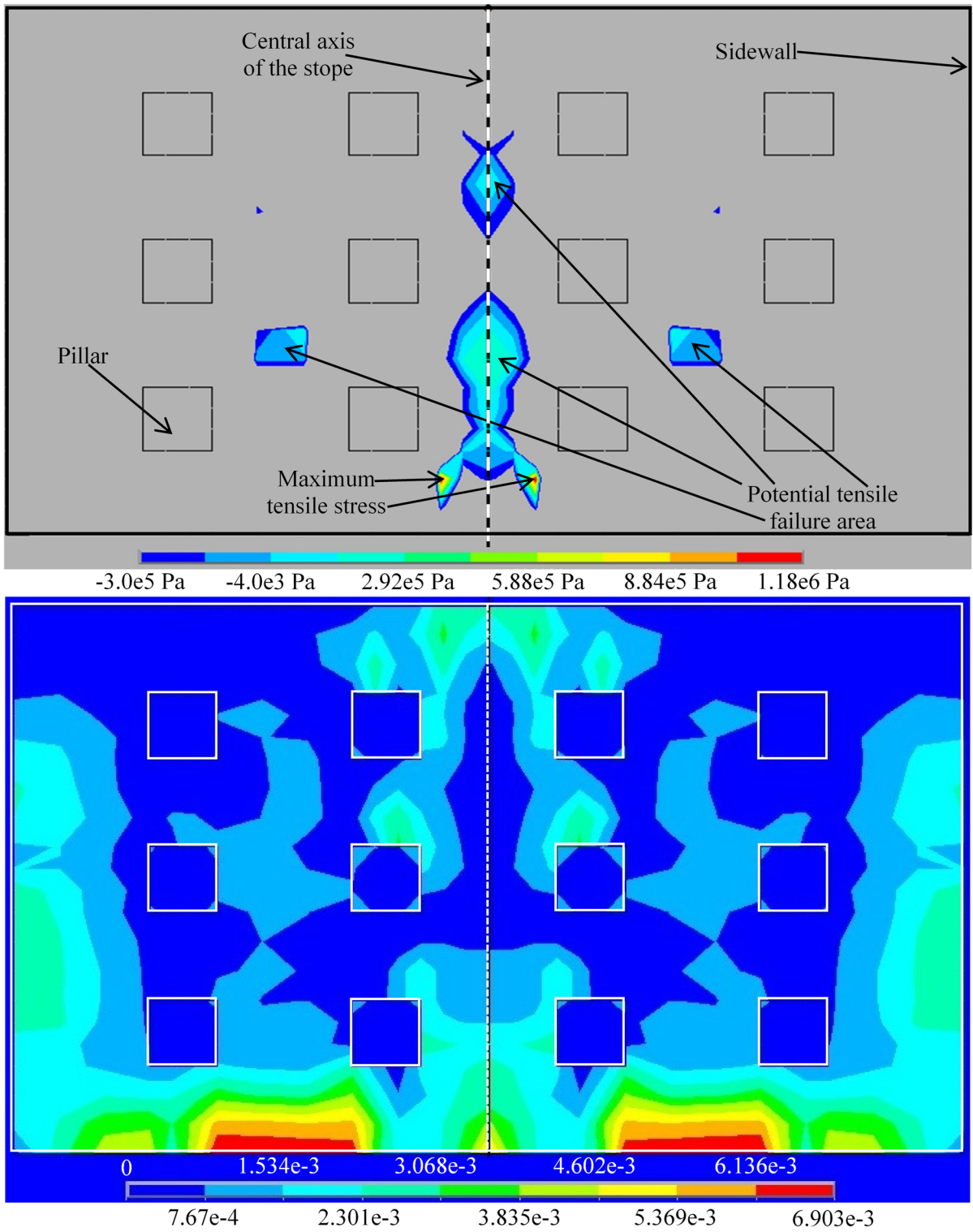


Fig. 21 The potential tensile failure area and equivalent plastic strain distribution in the roof

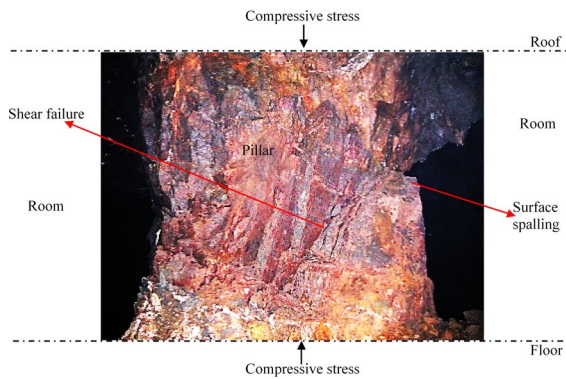


Fig. 22 The yielding and compressive failure of a carbonaceous limestone pillar

Subsequently, the shear failure zone extends to the pillar inside until the pillar is completely unstable and crushed.

5.4.2 Analysis of the roof instability mechanism

As the mining continues, the tensile deformation zone first appears in the roof, and its area and tensile stress increase continuously. If the tensile stress of the roof exceeds the tensile strength of rock mass, the roof will have tensile failure and induce tensile cracking. Finally, the roof will collapse. The stope width is continuously enlarged as the mining continues. Meanwhile, the vertical ground stress gradually transfers to the top and bottom of the pillar, and stress concentration occurs in the pillar and the contact zone between the pillar and the roof. The stress concentration intensity is related to the buried depth,

stope structural parameters, and regional tectonics. The greater the buried depth and span of stope, the more serious the stress concentration and the greater the possibility of pillar and roof failure (see Fig. 23). If the stress exceeds the ultimate bearing capacity of the rock mass, the roof will cave, and the wall will collapse.

6 Engineering application: underground stope structural parameters optimization

6.1 Optimization of the stope structural parameters

Based on the stope stability analysis results in Sect. 5, the pillar size and the room size for different stope heights are optimized to ensure the safety and stability of the stope. The stope height of the Baiyang mine section is between 2.5 and 4.5 m. Under three fixed stope's heights, the self-developed constitutive algorithm for isotropic softening plastic materials based on the unified strength theory is used to simulate the excavation of stope with different structural parameters to obtain the optimal size of the room and pillar. The orthogonal experimental design method is adopted to select the stope parameters, and the schemes of the stope structural parameters are obtained using the $L9(3^4)$ orthogonal table (see Table 2).

The same grid size is used to mesh the model and ensures comparability between different schemes. The tetrahedral 8-node element is used to partition the mesh, and the self-developed elastic–plastic constitutive algorithm in Sect. 3 is used to simulate the

Fig. 23 Analysis of the stope instability mechanism

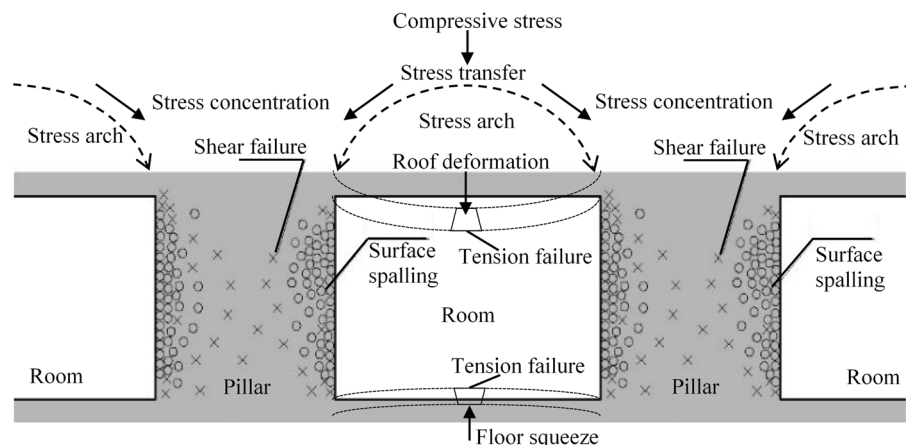


Table 2 The schemes of the stope structural parameters

Sequence number	Mining height/m	Square pillar width/m	Row spacing interval/m	Column spacing interval/m
1	2.5	2	2	4
2		3	3	5
3		4	4	6
4	3.5	2	3	6
5		3	4	4
6		4	2	5
7	4.5	2	4	5
8		3	2	6
9		4	3	4

stope excavation. In the study of scheme optimization, the most important thing is to choose the relevant characteristic quantity for comparison. Because the rock mass has feeble resistance to tensile stress, the maximum tensile stress in the roof, the maximum compressive stress in the pillar, and the maximum equivalent plastic strain are selected as the key criteria for the comparative study of different schemes.

6.2 Comprehensive analyses of optimization results of the stope structural parameters

The key criteria for the comparative study of different schemes are demonstrated in Fig. 24, Figs. 25, and 26. The calculation results of the fourth scheme are not convergent. Its pillar and roof are seriously deformed and become extremely unstable. The stability evaluation of the pillar in the figures shows that the overall stability of the pillar is higher if the pillar width is greater than 4 m. The roof stability analysis in the figures shows that if the room width is larger than 4 m, the stope roof is unstable.

According to the above analysis, the optimal structural parameters of stope are as follows: the mining height is between 2.5 and 4.5 m; the pillar width is 4 m; the column spacing is 4 m; the row spacing is between 3 and 4 m. The plastic deformation of the roof is large and the stability is not very high, so more attention should be paid to the safety monitoring of the roof.

Combined with the geological engineering conditions of the Baiyang mine section, the optimized structural parameters are applied to determine the sizes of the room and pillar. The design stope height is 4 m, the reserved pillar diameter is 4 m, the row spacing is 3 m, the column spacing is 4 m, the stope length is 40 m, and the stope width is 25 m. The stope layout is along with the inclination, and the pillars between each adjacent stope are kept 5 m wide. The field investigation results in the mining stope are as follows: 1. Most pillars are stable. However, the joints and fissures of some pillars are very developed, bringing about spalling and caving problems. 2. The roof and sidewall are stable, and there are no large dangerous rocks broken on the exposed surface of the roof. 3. The profile size of the pillar is difficult to guarantee, its centerline is not vertical, and its surface is uneven.

The optimized structural parameters improve the stability of the whole stope and realize the safe production of underground mining. Because of the poor stability of the surrounding rock in the Baiyang mine section, if the room-pillar method is continued to be used, the exposed area of the room may not be too large, which is less than 50 m². Some orebodies must be reserved as pillars, and the diameter of the pillars should be at least 4 m. For large stopes, the mining time is longer, so it is necessary to support the roof or keep artificial pillars. Besides, the stope height may not be too high, and 3.5 m is appropriate.

Fig. 24 The maximum tension stress of the pillar and roof

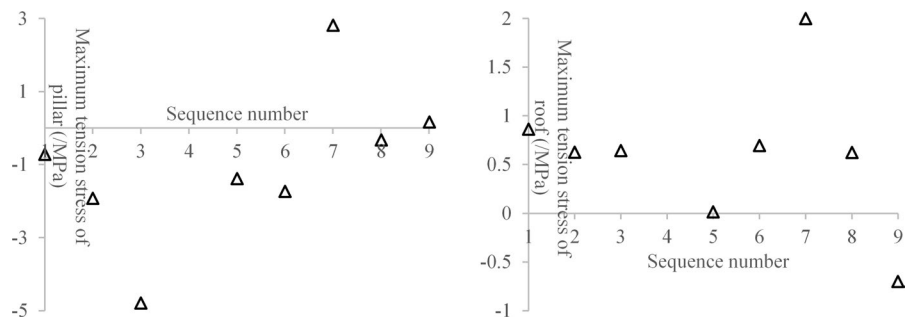


Fig. 25 The minimum principal stress of the pillar and roof

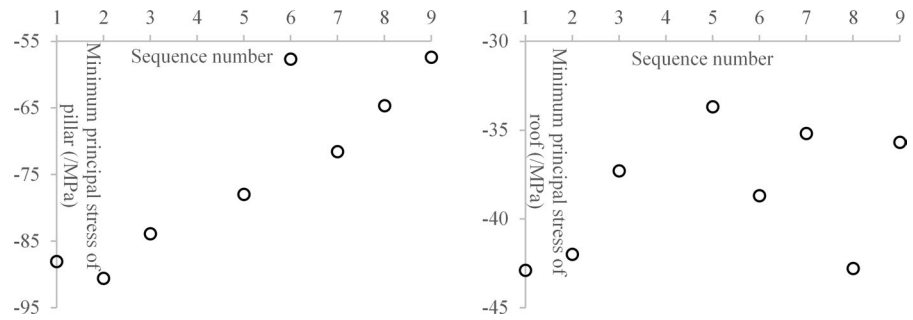
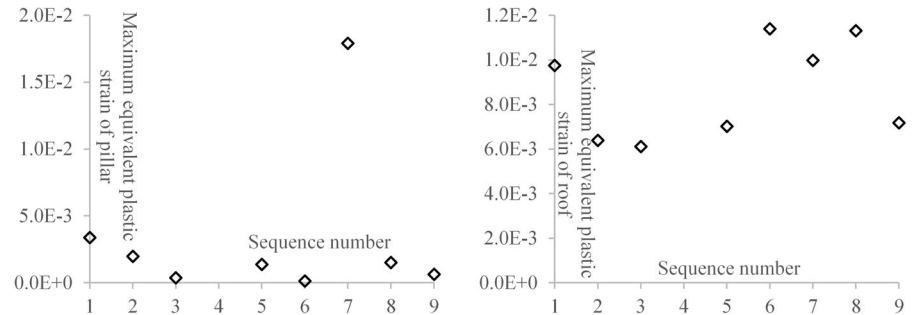


Fig. 26 The maximum equivalent plastic strain of the pillar and roof



7 Conclusion

The single-shear strength theory does not correctly consider the influence of intermediate principal stress. Moreover, the classical triple-shear strength theory does not consider the effect of stress angle on material strength. The calculated strength of both theories deviates from the experimental results, leading to conservative budgets. The unified strength theory can solve these problems. It has established a mathematical expression that can reasonably reflect the piecewise effect of intermediate principal stress on material strength, which cannot be expressed by a single-shear strength theory. Moreover, it contains many frequently used strength theories, and its yielding surface includes the convex and concave types, which can be widely applied to all kinds of materials. Using the unified strength theory can further improve the economic benefits of strength design. Additionally, the piecewise linear unified strength theory is more suitable for rock material since it has the simplest and most effective mathematical equations.

Therefore, a plastic constitutive algorithm for isotropic softening materials based on the unified strength theory was developed for rock engineering. Furthermore, the combination method of the

semi-implicit return mapping algorithm and the Aitken accelerated iteration scheme was applied to calculate the plastic deformation and the consistent tangent modulus. The self-developed constitutive algorithm was used to simulate the elastic–plastic excavation of a deep-lying circular tunnel. The numerical simulation results agreed with the theoretical solution and verified the correctness of the self-developed constitutive algorithm. The numerical experiment showed that the combination method of the semi-implicit return mapping algorithm and the Aitken accelerated iteration scheme can simplify the solution of the stress and the consistent tangent modulus. Besides, the combination method overcame the stress-deviating problem and avoided calculating the partial derivative of the plastic flow vector. The algorithm is simple and easy to be generalized.

Based on the mining practice of the gently inclined thin ore body in the Bainiuchang mine and its complex buried depth conditions, the self-developed constitutive algorithm was used to study the stabilities of the stope. Furthermore, the structural parameters of the stope were optimized. The results of stope stability analysis and structural parameters optimization provided a reliable scientific basis for the mining design and decision of Bainiuchang mine.

This study closely combined the research results with engineering applications, guided the safe and efficient production of mining, ensured the safety of underground stope, and achieved the expected goals. The optimization research and application of stope structural parameters have achieved complete success.

Author contributions Dr. Ke contributed to the study conception and design. Material preparation, data collection and analysis were performed by Dr. Ke. The first draft of the manuscript was written by Dr. Ke and all authors commented on the final version of the manuscript.

Funding The Young Scientists Fund of the National Natural Science Foundation of China (Grant No. 42202302). The Young Scientists Fund of the National Natural Science Foundation of Fujian province of China (Grant No. 2021J05104).

Data availability No datasets were generated or analysed during the current study.

Declarations

Conflict of interest The authors declare no competing interests.

Ethical approval All research activities were conducted in accordance with the ethical guidelines and principles outlined by the Committee on Publication Ethics.

Consent to publish All individuals involved in this study have provided their consent for the publication of the study findings. Any personal or identifying information that could potentially compromise privacy has been carefully removed or anonymized.

Open Access This article is licensed under a Creative Commons Attribution-NonCommercial-NoDerivatives 4.0 International License, which permits any non-commercial use, sharing, distribution and reproduction in any medium or format, as long as you give appropriate credit to the original author(s) and the source, provide a link to the Creative Commons licence, and indicate if you modified the licensed material. You do not have permission under this licence to share adapted material derived from this article or parts of it. The images or other third party material in this article are included in the article's Creative Commons licence, unless indicated otherwise in a credit line to the material. If material is not included in the article's Creative Commons licence and your intended use is not permitted by statutory regulation or exceeds the permitted use, you will need to obtain permission directly from the copyright holder. To view a copy of this licence, visit <http://creativecommons.org/licenses/by-nc-nd/4.0/>.

References

- Chen F, Wang YC, Li YH, Jiang W (2022) Investigation on the collapse mechanism of overlying clay layer based on the unified strength theory. *KSCE J Civ Eng* 26(9):3734–3740
- Gao F, Li SQ (2023) Elastic-plastic analysis of circular tunnel based on unified strength theory and considering multiple plastic zones. *Adv Mech Eng*. <https://doi.org/10.1177/16878132221146392>
- Gao YF, Tao ZY (1993) Examination and analysis of true triaxial compression testing of strength criteria of rock. *Chin J Geotech Eng* 15(4):26–32
- Hajiabdolmajid V, Kaiser PK (2003) Brittleness of rock and stability assessment in hard rock tunneling. *Tunn Undergr Space Technol* 18(1):35–48
- Hajiabdolmajid V, Kaiser PK, Martin CD (2002) Modelling brittle failure of rock. *Int J Rock Mech Min Sci* 39:731–741
- Hajiabdolmajid V, Kaiser PK, Martin CD (2003) Mobilised strength components in brittle failure of rock. *Géotechnique* 53(3):327–336
- Hoek E (1983) Strength of jointed rock masses. *Géotechnique* 33(3):187–223
- Hoek E, Brown ET (1997) Practical estimates of rock mass strength. *Int J Rock Mech Min Sci* 34(8):1165–1186
- Hoek E, Wood D, Shah S (1992) A modified Hoek–Brown criterion for jointed rock masses. In: *Proceeding of the ISRM symposium on rock characterization*. British Geotechnical Society, London, pp 209–214
- Hu XR, Yu MH (2004) New research on failure criterion for geomaterial. *Chin J Rock Mech Eng* 23(18):3037–3037
- Jing F, Sheng Q, Zhang YH, Liu YK (2011) Study advance on in-site geostress measurement and analysis of initial geostress field in China. *Rock Soil Mech* 32(S2):51–58
- Labuz JF, Zang A (2012) Mohr–Coulomb failure criterion. *Rock Mech Rock Eng* 45(6):975–979
- Li HZ, Xu JT, Zhang ZL, Song L (2023) A generalized unified strength theory for rocks. *Rock Mech Rock Eng* 56(11):7759–7776
- Liu H, Kong D, Zhao Y, Zhang L (2023) Active earth pressure of finite soil based on twin-shear unified strength theory. *Soil Mech Found Eng* 60(3):259–267
- Miao P, Chen YM, Zheng ZZ (2024) Calculation method for ultimate bearing capacity of reinforced concrete beams based on unified strength theory. *Int J Mater Product Technol*. <https://doi.org/10.1504/IJMPT.2024.136843>
- Mogi K (1966) Pressure dependence of rock strength and transition from brittle fracture to ductile flow. *Bull Earthq Res Inst* 44:215–232
- Mogi K (1967) Effect of the intermediate principal stress on rock failure. *J Geophys Res* 72(20):5117–5131
- Mogi K (1971) Fracture and flow of rocks under high triaxial compression. *J Geophys Res* 76(5):1255–1269
- Qiao L, Gao W, Li Y, Yang ZJ (2012) Improved CWFS model for hard rocks and its application to stability analysis of high rock slope. *Chin J Rock Mech Eng* 31(S1):2593–2600
- Shen ZJ (1995) Summary on the failure criteria and yielding functions. *Chin J Geotech Eng* 17(1):1–8

- Singh B, Goel RK, Mehrotra VK, Garg SK, Allu MR (1998) Effect of intermediate principal stress on strength of anisotropic rock mass. *Tunn Undergr Space Technol* 13(1):71–79
- Sun ZY, Zhang DL, Fang Q, Dui GS, Chu ZF (2022) Analytical solutions for deep tunnels in strain-softening rocks modeled by different elastic strain definitions with the unified strength theory. *Sci China-Technol Sci* 65(10):2503–2519
- Walton G, Arzúa J, Alejano LR, Diederichs MS (2015) A laboratory-testing-based study on the strength, deformability, and dilatancy of carbonate rocks at low confinement. *Rock Mech Rock Eng* 48(3):941–958
- Wang CW, Liu XL, Song DQ, Wang EZ, Zhang JM (2023) Elasto-plastic analysis of the surrounding rock mass in circular tunnel using a new numerical model based on generalized nonlinear unified strength theory. *Comput Geotech*. <https://doi.org/10.1016/j.compgeo.2022.105163>
- Wu Y, Zhao C, Zhao CF, Liu FM, Zhang JQ (2022) Modeling of compaction grouting considering the soil unloading effect. *Int J Geomech*. [https://doi.org/10.1061/\(ASCE\)GM.1943-5622.0002384](https://doi.org/10.1061/(ASCE)GM.1943-5622.0002384)
- Xiong ZM, Lin LY, Sun QR, Chen X (2023) Study of the unified strength theory for seismic response of frame building on loess considering soil-structure interaction. *Struct Des Tall Spec Build*. <https://doi.org/10.1002/tal.2038>
- Yu MH (2004) Unified strength theory and its applications, 1st edn. Springer, Berlin
- Yu MH (2007) Linear and nonlinear unified strength theory. *Chin J Rock Mech Eng* 26(4):662–662
- Yu MH (2018) Unified strength theory and its applications, 2nd edn. Springer, Berlin
- Yu MH, Li JC (2012) Computational plasticity: with emphasis on the application of the unified strength theory and associated flow rule. Springer and ZJU Press, Berlin
- Yu MH, Zan YW, Fan W, Zhao J, Dong ZZ (2000) Advances in strength theory of rock in 20 century—100 years in memory of the Mohr-Coulomb strength theory. *Chin J Rock Mech Eng* 19(5):545–550
- Yu MH, Zan YW, Zhao J, Yoshimine M (2002) A unified strength criterion for rock material. *Int J Rock Mech Min Sci* 39(8):975–989
- Yu MH, Yoshimine M, Qiang HF, Zan YW, Xiao Y, Li LS, Sheng ZM (2004) Advances and prospects for strength theory. *Eng Mech* 21(6):1–20
- Yu MH, Ma GW, Qiang HF, Zhang YQ (2006) Generalized plasticity: both for metals and geomaterials. Springer, Berlin
- Yu MH, Ma GW, Li JC (2009) Structural plasticity: limit, shakedown and dynamic plastic analyses of structures. Springer and ZJU Press, Berlin
- Zan YW, Yu MH (2013) Generalized nonlinear unified strength theory of rock. *J Southwest Jiaotong Univ* 48(4):616–624
- Zan YW, Yu MH, Wang SJ (2002) Nonlinear unified strength criterion of rock. *Chin J Rock Mech Eng* 21(10):1435–1441
- Zan YW, Yu MH, Zhao J, Yoshimine M (2004) Nonlinear unified strength theory of rock under high stress state. *Chin J Rock Mech Eng* 23(13):2143–2148
- Zeng KH, Ju HY, Zhang CG (2011) Elastoplastic unified solution for displacements around a deep circular tunnel and its comparative analysis. *Rock Soil Mech* 32(5):1315–1319
- Zhang B, Sun QL (2023) Upper bound analysis of the anti-seismic stability of slopes considering the effect of the intermediate principal stress. *Front Earth Sci*. <https://doi.org/10.3389/feart.2022.1023883>
- Zhao DA, Chen ZM, Cai XL, Li SY (2007) Analysis of distribution rule of geostress in China. *Chin J Rock Mech Eng* 26(6):1265–1271
- Zienkiewicz OC, Pande GN (1977) Some useful forms of isotropic yield surfaces for soil and rock mechanics. In: Gudehus G (ed) *Finite elements in geomechanics*. Wiley, London, pp 179–190

Publisher's Note Springer Nature remains neutral with regard to jurisdictional claims in published maps and institutional affiliations.